

**QUANTITATIVE DETERMINATION OF HYPOXIA IN TUMOURS
USING MRI FOR ADAPTIVE RADIOTHERAPY**

Shagufta Maimona Mubeen

Bachelor of Engineering
Computer Engineering



Department of Science and Engineering
Macquarie University

June 5, 2017

Academic Supervisor: Professor Yves De Deene



ACKNOWLEDGMENTS

Firstly, I would sincerely like to thank my supervisor, Professor Yves De Deene and co-supervisor Mahdiah Moghari for their patience, support and guidance during my project.

I would also like to thank Charmaine, my manager at AstraZeneca for being so supportive and encouraging in this entire journey. Thank you for always encouraging me to do my best.

Thank you to my parents, for being my backbone and always being there for me. Your love and support brought me to this stage

A huge thank you to Umar. Thank you for being my biggest motivator and pillar of support in this journey.

Lastly, I would like to thank Hala for her help and guidance in this thesis.



STATEMENT OF CANDIDATE

I, (Shagufta Maimona Mubeen), declare that this report, submitted as part of the requirement for the award of Bachelor of Engineering in the Department of Electronics Engineering, Macquarie University, is entirely my own work unless otherwise referenced or acknowledged. This document has not been submitted for qualification or assessment to any academic institution.

Student's Name: Shagufta Maimona Mubeen

Student's Signature: Shagufta Maimona Mubeen

Date: 16th June, 2017



ABSTRACT

Hypoxia can be defined as the condition in which the body or areas of the body are lacking in adequate supply of oxygen at the tissue level. The condition is not common in normal functioning tissue but frequently appears in tumours and is often described as a characteristic feature of tumours.

Tumour hypoxia can originate by means of perfusion, diffusion or anaemia related causes. It is known that the vasculature of tumours is distorted due to inefficient blood flow inside the tumour. As a result the oxygenation status of a tumour varies considerably.

It is known that hypoxic regions are three to four times more resistant to radiotherapy as compared to normoxic tumour cells. Therefore in the treatment of cancer, treatment plans need to be designed that take into consideration tumour specific biological data on an individual basis. In order to achieve this more quantitative data is needed such as cellular density, oxygen concentrations, vascular density blood fractions and so on. Therefore, this thesis discusses the methods involved in the quantitative determination of hypoxia in tumours using Magnetic Resonance Imaging (MRI) so that efficient radiotherapy may be administered to cancer patients.



Contents

Acknowledgments	iii
Abstract	vii
Table of Contents	ix
List of Figures	xi
List of Tables	xiii
1 Introduction	1
1.1 Motivation	1
1.2 Project aim	2
1.3 Thesis summary	3
2 Literature Review: Basic principles of an MRI	5
2.1 Overview	5
2.2 Short historical overview	5
2.3 Basic principles of MRI	7
2.3.1 Spin physics	7
2.3.2 Spin relaxation- Bloch equations	11
2.3.3 Relaxation times	14
2.3.4 Transverse relaxation time	17
2.3.5 Longitudinal relaxation time	19
2.4 Quantitative Magnetic Resonance Imaging	21
2.5 Multi-nuclear MRI	23
2.5.1 Fluorine-19 (^{19}F)	23
2.6 MRI hardware	24
3 Literature Review: Cancer, hypoxia and oximetry	27
3.1 Overview	27
3.2 Oncogenesis	27
3.3 Cancer epidemiology	28
3.4 Cancer treatment	30

3.5	Hypoxia	31
3.5.1	Origin of hypoxia	32
3.5.2	Effects of hypoxia	34
3.5.3	Consequences for cancer treatment	36
3.6	Oximetry	37
3.6.1	Magnetic resonance imaging as a measuring technique	38
3.6.2	DCE MRI	38
3.7	Conclusion	38
4	Project model and methods	41
4.1	Introduction	41
4.2	Project overview	41
4.3	Experimental procedure	42
4.3.1	Phantom construction	43
4.3.2	MRI scanning of the phantom	44
4.3.3	Acquiring DICOM images	44
4.4	Computational study	46
4.4.1	Sorting DICOM images	46
4.4.2	Curve fitting and T_1 mapping	47
4.4.3	Concentration map	48
4.4.4	Dynamic response	50
5	Results and Discussion	51
5.1	Introduction	51
5.2	Curve fitting and T_1 map	51
5.3	Concentration map	53
5.4	Dynamic Response	54
5.5	Conclusion	57
6	Conclusion and future works	59
6.1	Conclusion	59
6.2	Future works	60
	Bibliography	62
	Appendix A More about hypoxia	65
	Appendix B MATLAB Code: Renaming files	71
	Appendix C MATLAB Code: Curve fitting and T_1 mapping	73
	Appendix D MATLAB Code: Concentration map and Dynamic response	77
	Appendix E Consultation Meetings Attendance Form	83

List of Figures

2.1	Cartesian coordinate system [8].	8
2.2	Zeeman diagram [8].	10
2.3	Motion of spin [8].	11
2.4	Magnetisation orientation [8].	12
2.5	Spin orientation [8].	13
2.6	Transverse relaxation [7]	16
2.7	Orientation after RF pulse [15].	18
2.8	Quantitative T_1 , T_2 , and T_2^* maps of the lower midbrain. [21].	22
2.9	The MRI scanner consists of three main components: (1) The DC magnet which produces the static magnet field, (2) RF coils that enables the creation of excitation pulses and reception of the NMR signal and (3) the gradient coils which create magnetic fields of varying amplitudes spatially in any of the three orthogonal directions. [1].	25
3.1	5-year relative survival from all cancers combined, by sex, 1984-1988 to 2009-2013 [24]	29
3.2	The figure illustrates the diffusion of oxygen from a capillary in to tumour tissue. Radial oxygen diffusion distances are restricted by oxygen consumption and as a result the oxygen supply becomes insufficient at greater distances. Cells become hypoxic, but still viable when oxygen concentration is low and necrotic when the oxygen concentration becomes zero. [24]	34
3.3	The figure shows a schematic representation of the effects of hypoxia on tumour progression and resistance to therapy [7]	35
4.1	Flow chart of the project structure and the tasks involved	42
4.2	The experimental setup for MRI scanning [9]	43
4.3	(left) Side view of the phantom with connections to the inner compartment at the sides of the filter and connections to the outer compartment filled with hydrogel. (right) Opened entrance part of the inner compartments of the haemodialysis filter showing the hollow fibres. [19]	44
4.4	The signal intensity (S_i) values outside and inside the phantom. The values in the original file have an offset of 2048, the modified file subtracts the offset to obtain the actual contrast.	45

4.5	MATLAB Code for Curve fitting using Eq. 4.1	48
4.6	A schematic representation of the points from which the concentration maps were derived. The borders around each point indicate the regions which were used for each respective point to calculate the dynamic response.	50
5.1	(a) Represents point outside the phantom (b)-(d) Represents points inside the phantom.	52
5.2	(a) T_1 map before contrast agent was injected. (b) T_1 map after contrast agent. The contrast agent shortens T_1 values.	53
5.3	Change in concentration of Gd-DTPA over time at various points inside the phantom	55
5.4	Dynamic response at various points inside the phantom as marked in Fig. 4.6	56
6.1	A schematic representation of the experimental setup of a phantom for the quantitative ^{19}F MRI-oximetry method [19]	61

List of Tables

1.1	Thesis outline (chapter-wise)	3
2.1	Spin quantum numbers and gyromagnetic ratios for some nuclei	9
2.2	T_1 and T_2 relaxation times for various biological tissue at a magnetic field of 1.5T [7]	17
3.1	The table shows the estimated most common cancers diagnosed in 2017 in Australia. [24]	29
4.1	Standard imaging parameters during MRI scanning	46



Chapter 1

Introduction

1.1 Motivation

In multicellular organisms the amount of cells in the organism is monitored and regulated by the bodily processes of cell division and self-elimination. Additionally, other mechanisms in the body control cell differentiation and monitor and maintain tissue integrity by limiting cells to stay within their tissue boundaries. But however, when genetic mutations occur they allow cells to escape these control mechanisms and boundaries. As a consequence, the process of cell self-elimination collapses and an uncontrollable process of cell division takes place, formation of cancerous tumours. When cancer arises the cancer cells become variant to normal cells in cell structure and anatomy and tend to survive outside tissue boundaries which leads to further complications such as metastasis.

Cancer is one of the leading causes of death worldwide and is responsible for nearly 8.8 million deaths that occurred in 2015 [3]. Cancer occurs in individuals due to various reasons, some lifestyle related such as heavy tobacco and alcohol use, poor nutrition, lack of physical activity and others, while other reasons are genetically related. Individuals have high chances of survival of being cured if they avoid risk factors that are related to lifestyle as well as if they are diagnosed early and treated with proper methods.

In the treatment of cancer various factors need to be taken into account. These factors include things such as the nature of the tumour, its anatomical location in the body, the severity or clinical stage of the tumour and the overall health of the patient. The treatment of cancer is a multidisciplinary approach whereby it is a combination of the three main cancer treatment mediums, i.e. surgery, chemotherapy and radiotherapy and it therefore a cooperation of several clinical departments.

Surgery is not always an ideal option as remnants of tumours can still remain within the individual. Chemotherapy on the other hand is a systemic treatment, i.e. it affects the whole body. Chemotherapy involves the administration of chemical and organic molecules which kill all the rapidly dividing cells in the human body regardless of the

nature of the cell. This means that the rapidly dividing tumour cells are directly targeted by chemotherapy but so are the other fast dividing cells such as hair follicles, skin and gastrointestinal cells.

Radiotherapy utilises ionising radiation for the purpose of damaging tumour cells. The ionising radiation comes from either a linear accelerator or radioactive sources. The most frequently used and common form of radiotherapy is external beam radiotherapy. External beam radiotherapy focuses on outputting radiation doses into malignant tumour tissue. The radiation doses aim to be highly uniform and also preserve the neighbouring healthy tissue in the body. However up until recently, in radiotherapy tumours were considered as solid homogenous bodies that are invariant over time. This is actually not the case because tumours have been realised to be biologically heterogeneous. They are composed of different regions, where some regions contain proliferating cells, while some regions contain necrotic cells. Tumours also develop irregular vascular structures (angiogenesis) and as a result the oxygenation status of tumours vary considerably. Angiogenesis is one of the main causes of hypoxic and anoxic regions in tumour cells [9].

It is known that hypoxic cells in tumours are three to four times more resistant to radiotherapy as compared to normoxic tumour cells. Radiotherapy is carried out in fractions whereby the patient receives small incremental doses daily over a period of weeks. In this time period the tumour changes as a response to the treatment but also due to other factors such as re-oxygenation, repopulation, redistribution and tumour shrinkage. All of these factors have the potential to modify the initial spatial and functional pattern on which the prescribed radiation dose distribution is based. Therefore, treatment plans need to be designed that take into consideration tumour specific biological data on an individual basis. In order to achieve this more quantitative data is needed such as cellular density, oxygen concentrations, vascular density blood fractions and so on [9].

1.2 Project aim

The aim of the project was ultimately to map oxygen concentration in tumour tissue in vivo so that efficient radiotherapy may be administered to cancer patients. The correlation between blood flow, vascular density, oxygen consumption and oxygen concentration in tissue was experimentally modelled in vitro. The experimental model was composed of bio-perfusion phantom that is comprised of small capillaries that are perfused with blood mimicking fluid. The phantom was scanned on a clinical MRI scanner with Dynamic Contrast Enhanced (DCE) MRI sequences and can be used a way to validate experimental methods to map oxygen concentration with MRI. The experimental model can then be used a test model of computational modelling that takes the vascularisation and diffusion of oxygen into tissue in consideration.

Eventually for in vivo measurements, Fluor-containing artificial blood substitutes and would act as oxygen markers in patients. Using DCE MRI the permeability, size and density of capillaries can be calculated and hence a computational model of radiobiological effectiveness incorporating the effect of oxygen on cell survival can be established.

Initially, as a first step the bio-perfusion phantom is to be injected with a contrast agent, Gd-DTPA in order to understand the dynamics of the system before moving onto Fluorine-19 (^{19}F). From the DCE-MRI scanning of the phantom we are to produce quantitative T_1 maps and map the concentration (perfusion) of the contrast agent over time. This would be a milestone in acquiring oxygen concentration maps using ^{19}F MRI oximetry.

1.3 Thesis summary

In this section, a short introduction about the motivation behind the project is outlined. The project aim is also discussed in detail. The literature review is contained in Chapter 2 and Chapter 3. Chapter 2 provides a thorough explanation about the basic principles of MRI and associated concepts while Chapter 3 discussed cancer, hypoxia and oximetry. Chapter 4 is based on the system model and it provides a detailed study about the project overview and the various methods that were carried out, i.e. the experimental procedure and the computational study. Chapter 5 presents the results and an interpretation and discussion of the results. Chapter 6 concludes and summarises the thesis followed by a discussion of the future work.

Chapter 1	Introduction about the project and motivation
Chapter 2	Detailed background information about the physics behind MRI
Chapter 3	Background information about hypoxia and its effect in cancer therapy
Chapter 4	System model: Describes all the tasks carried out in the project
Chapter 5	Results and interpretation
Chapter 6	Summary of thesis and future work

Table 1.1: Thesis outline (chapter-wise)

Chapter 2

Literature Review: Basic principles of an MRI

2.1 Overview

MRI is a powerful imaging technique that is used in the medical field. A key distinguishing factor between MRI and other imaging techniques is that MRI does not use ionising radiation, instead it uses a strong magnetic field and is used in conjunction with electromagnetic radio frequency (RF) pulses. MRI has now become a vital part of medical examinations, where a detailed view of complex internal structures is required.

In order to have a thorough understanding of the information presented in this work, this chapter provides a summary of the basic principles of magnetic resonance imaging as well as a short historical review. There is a particular focus on the physics involved in MRI and relaxation times. Next, we discuss what quantitative magnetic resonance is and the need for it, followed by a discussion about multi-nuclear MRI. Finally, a brief summary about the MRI hardware components is presented.

2.2 Short historical overview

Nuclear Magnetic Resonance (NMR) was first described in 1938 by Isidor I. Rabi, a professor at Columbia who observed nuclear magnetic resonance by realising that atomic nuclei emit radio waves after they are exposed to a strong magnetic field. Soon after World War II, NMR was noticed in solids and liquids by two teams independently led by Edward Purcell at MIT in Harvard and Felix Bloch at Stanford.

Purcell and his team filled an electromagnetic cavity with solid paraffin and placed the device in an electromagnet. As they applied an oscillating current to the cavity they noted that after a certain point there was an increase in the absorption of radiation. This verified

their prediction of the existence of nuclear magnetic resonance of hydrogen nuclei at a specific field strength and frequency. At the same time at Stanford, Felix Bloch and his team had demonstrated NMR in their experiment by recording a current induced in a nearby coil from rotation of a magnetisation vector.

Felix and Bloch shared the Nobel Prize in 1952 for developing a method to measure NMR. They had both discovered that the nuclei of atoms behaved like tiny, spinning bar magnets and when these magnets were placed in a strong magnetic field the atomic nuclei had a tendency to align with it. Felix and Bloch both noticed that when they would emit a pulse of radio waves the nuclei would absorb this energy causing them to become in an excited state and change direction. And the time it would take for the nuclei to become relaxed and return to their original state was measured. In doing so, it became possible to determine the molecular composition of different chemical compounds because every atomic nucleus resonates at a unique characteristic radio frequency in a given magnetic field [5].

Then in the late 1960s Raymond Damadian, a physician working at the State University of New York's Medical Centre in Brooklyn, discovered that the hydrogen nuclei of water in cancerous and healthy tissues were showing significant variations in relaxation times. Around the same time Paul Lauterbur came up with the idea- which is now the basis of how MRI scanners operate- to superimpose small variations/gradients in the uniform magnetic field. It became known that changing the field strength would affect the resonance frequency of nuclei in direct proportion and this can be used to construct an image or encode spatial information. The intensity of the resonance signal at a certain frequency was indicative of the quantity of the nuclei at a specific location. Being able to encode the sequence, spatially, was a ground breaking discovery that enabled MRI, prior to this there were no other applications that could successfully detect hydrogen nuclei.

In 1973, Dr. Lauterbur, a chemist, together with Peter Mansfield a physicist, produced the first NMR image of a test tube. At the same time Damadian was in the process of obtaining a patent in which he described the concept of NMR and illustrated the main parts of his proposed MRI machine. By 1978 Damadian had built the first MRI scanner with the help of his post-doctoral students, Michael Goldsmith and Larry Minkoff at New York's Downstate Medical Centre. By this time, they had acquired the first MRI scan of a healthy human body and achieved the first MRI scan of the human body with cancer in 1978.

Later, Peter Mansfield improved the mathematics involved in the MRI process and invented the echo planar technique which made it possible for MR images to be produced within seconds. His work went on to become the basis of the current and fast MR imaging we have today [4].

2.3 Basic principles of MRI

In recent times MRI has become the most essential non-invasive imaging technique for several fields of engineering, biology and material science. MRI has revolutionised medicine with its unique features of non-ionising radiation and high spatial resolution of soft bodily tissues. MRI is based on the principles of NMR which deals with the interaction between an external magnetic field and a nucleus that possess's spin. Nuclear spin or else known as nuclear spin angular momentum, is one of the most crucial properties of atoms and is largely dependent on the atomic composition. Any element that contains an odd number of protons or neutrons has a naturally occurring isotope that possesses the spin characteristic. Therefore, these elements are capable of being examined using magnetic resonance.

2.3.1 Spin physics

Atoms are made up of three basic building blocks: protons, which have a positive charge, electrons which have a negative charge and neutrons which have no charge. In relation to MRI, the point of interest is the nucleus of the hydrogen atom in water.

The proton has four fundamental properties: charge, mass, angular momentum and magnetic momentum. When the total number of protons and neutrons is odd or the total number of protons is odd, a nucleus has an angular momentum (or spin). It is the spin of a nucleus which generates a magnetic field, which has a magnetic moment. As the nucleus is continually rotating about an axis at a constant rate paired with the charge of the nucleus it exhibits magnetic properties similar to a small bar magnet.

Now when an object is placed inside a magnetic field, B_0 , every proton begins to precess, or rotate perpendicular to the magnetic field. During precession the protons are slightly tilted away from the axis of the magnetic field, however the axis of precession remains parallel to the magnetic field, B_0 . The precession is carried out at a constant rate due to the interaction between the magnetic field and the spinning positive charge of the nucleus.

With respect to the Cartesian coordinate system the magnetic field, B_0 and the axis of precession are known to be aligned in the z direction of the plane. The direction of the magnetic dipole moment is plotted by a set of coordinates that are perpendicular and parallel to B_0 [8].

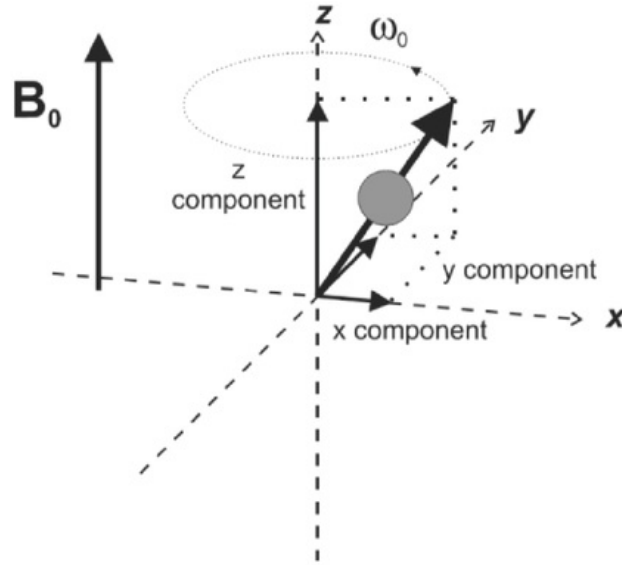


Figure 2.1: Cartesian coordinate system [8].

It is known that frequency of precession is proportional to the strength of the magnetic field and is expressed by the Larmor equation:

$$\omega_0 = \frac{\gamma B_0}{2\pi} \quad (2.1)$$

ω_0 is defined as the Larmor frequency and is expressed in megahertz, B_0 is the magnetic field that the proton is subjected to and is measured in Tesla, lastly γ is the gyromagnetic ratio, a constant that is unique for each nucleus.

Following the direction perpendicular to B_0 the spin remains the same, i.e. randomly distributed as they were outside the magnetic field which is irrespective of the time variation of each transverse component. Despite this process occurring there is still an absence of any net magnetisation perpendicular to B_0 . However, this is not in the case of the direction parallel to the magnetic field [8]. Due to the presence of an orientation that is associated with the precessional axis of the proton, that remains constant with time, there arises a constant, non-zero interaction (or coupling) between the proton and magnetic field, otherwise known as the Zeeman interaction.

In clinical MRI examinations, the nucleus of the Hydrogen (^1H) atom is taken into consideration. The proton of a H_2O water molecule is abundant naturally within the body.

Additionally, other nuclei such as ^{13}C , ^{19}F , ^{23}Na and ^{31}P may also be studied in Nuclear Magnetic Resonance (NMR), as in Tab. 2.1.

Table 2.1: Spin quantum numbers and gyromagnetic ratios for some nuclei

Nucleus	Net spin, I	$\gamma/2\pi$ (MHz/T)	Natural occurrence
^1H	$1/2$	42.58	$\approx 100\%$
^2H	1	6.54	0.015%
^{13}C	$1/2$	10.71	1.1 %
^{14}N	1	3.08	99.6%
^{19}F	$1/2$	40.08	$\approx 100\%$
^{23}Na	$3/2$	11.27	$\approx 100\%$
^{31}P	$1/2$	17.25	$\approx 100\%$

For the purpose of this thesis we will study the spin quantum number of ^1H and ^{19}F nuclei which is $I = \frac{1}{2}$ which means that their magnetic moment has two possible states: $+\frac{1}{2}\gamma\hbar$ and $-\frac{1}{2}\gamma\hbar$. When an external magnetic field, B_0 is applied, the discrete magnetic moments of a nucleus possess potential energy. Specifically, for nuclei with a spin of $\frac{1}{2}$, the potential energy splits into two levels:

$$E = -\mu B_0 = +\frac{1}{2}\gamma\hbar B_0, \quad \text{spin down, } I_z = -\frac{1}{2} \quad (2.2)$$

$$-\frac{1}{2}\gamma\hbar B_0, \quad \text{spin up, } I_z = +\frac{1}{2} \quad (2.3)$$

The splitting of this energy is called Zeeman interaction, it highlights that spins in two different orientations, i.e. parallel (or otherwise known as spin up) and antiparallel (known as spin down) have differing energies. Of the two spin orientations, the spin orientation that is parallel to the magnetic field is the one with the lower energy. The transition between these two energy levels are possible by means of absorption or emission of a photon with energy $\Delta E = \gamma\hbar B_0$. The angular frequency $\omega_L = \gamma B_0$ of the transition photons is the Larmor frequency.

Atomic nuclei do not occur individually, one-by-one but rather collectively, as a large number of spins. When the group of protons is placed in an external magnetic field and there is a large number of protons present, majority will be oriented in the direction parallel to B_0 rather than antiparallel to B_0 , i.e. there is an induced polarisation of the spin orientation by the magnetic field. The Boltzmann distribution is then used to determine the precise number of protons in each energy level. It is as follows:

$$\frac{N_-}{N_+} = e^{\frac{-\Delta E}{kT}} \quad (2.4)$$

Where N_- is the number of spins in the spin-down and N_+ , the number of spins in the spin-up state, k is Boltzmann's constant and T is the absolute temperature. The fractional excess of the protons at the lower energy state increases with the magnetic field strength and decreasing temperature.

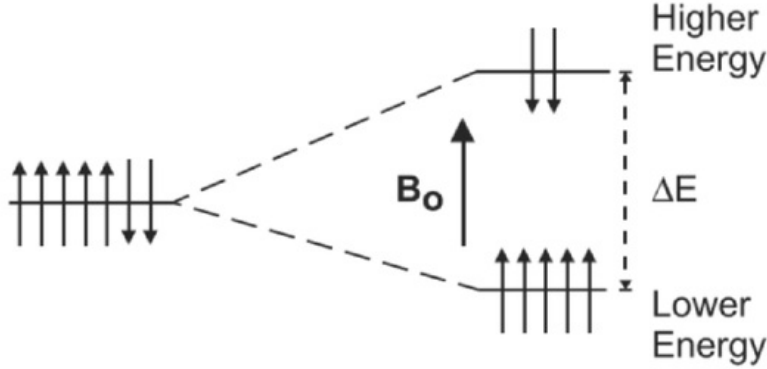


Figure 2.2: Zeeman diagram [8].

E is dependent on the magnetic field strength as well as the exact number of spins in each level. As the magnetic field strength increases so does the number of spins.

When protons in a tissue are at normal body temperature and subject to a magnetic field of 1.5 T, in the lower energy level there is an excess of protons within the tissue. The unequal distribution of protons in each energy level results in a vector sum that will be non-zero and will point parallel to the magnetic field. This means that the tissue will become polarized in the presence of B_0 and have a value M_0 which is the net magnetisation. The orientation of this net magnetisation follows the same direction as the magnetic field and is constant with respect to time. Tissues within the body have a magnitude which is proportional to the magnetic field, it is represented by:

$$M_0 = \chi B_0 \quad (2.5)$$

Where χ represents the magnetic susceptibility and M_0 aligned with the magnetic field with the absence of a transverse component is the normal configuration for the protons. This is the configuration of spin which has the lowest energy and is the arrangement which the protons will be naturally inclined to return to following any fluctuations or changes such as energy absorption. This induced magnetisation, M_0 , is the essential source of signal for all MR related experiments. Since all other factors are equal it is consequently

then that the greater the field strength. The greater the value of M_0 and thus the greater the potential MR signal.

A coordinate system is used to simplify the description of the motion of the spin as it continues to precess. The spin is said to be in a rotating frame of reference, or a rotating coordinate system. In this rotating frame of reference the coordinate system rotates about one axis while the other two axes vary with respect to time. For the purpose of MR experiments, the z axis is occupied by the rotating frame of reference which is parallel to the magnetic field and is the axis of rotation. The x and y axes are rotating at the Larmor frequency, ω_0 . When it is observed in this manner, the precessing spin is stationary in space with a fixed set of x, y and z coordinates but when an entire volume of a tissue is examined, i.e. a collection of protons the result will be an equal number of positive and negative x and y values with a slight excess of positive z values. When a vector sum on the protons is calculated, the x and y components total to zero and a non-zero, positive z component is left, which is in reality the net magnetisation, M_0 . M_0 does not vary with time, it is a fixed amplitude and is parallel to the main magnetic field. [15]

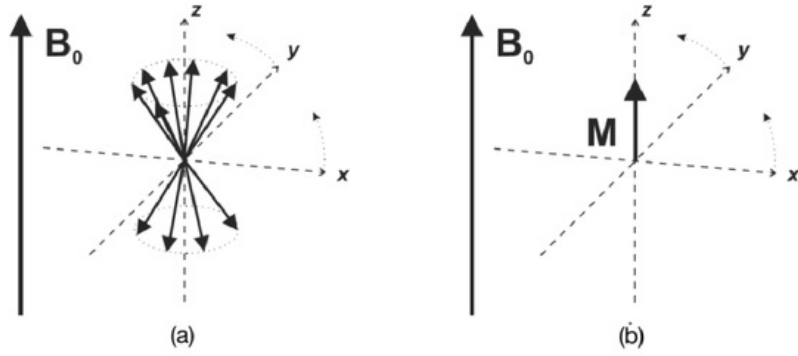


Figure 2.3: Motion of spin [8].

2.3.2 Spin relaxation- Bloch equations

When the spin magnetisation vector, (M), is placed in an external magnetic field, (B_0), the magnetisation vector experiences a torque. The equation for the magnetisation vector is:

$$\frac{dM}{dt} = \gamma.(M \times B) \quad (2.6)$$

When considering the above equation with respect to the x, y and z direction in a static magnetic field, B_0 , that is directed along the z-axis we follow the equations below:

$$\frac{dM_x}{dt} = \gamma M_y B_0 \quad (2.7)$$

$$\frac{dM_y}{dt} = -\gamma M_x B_0 \quad (2.8)$$

$$\frac{dM_z}{dt} = 0 \quad (2.9)$$

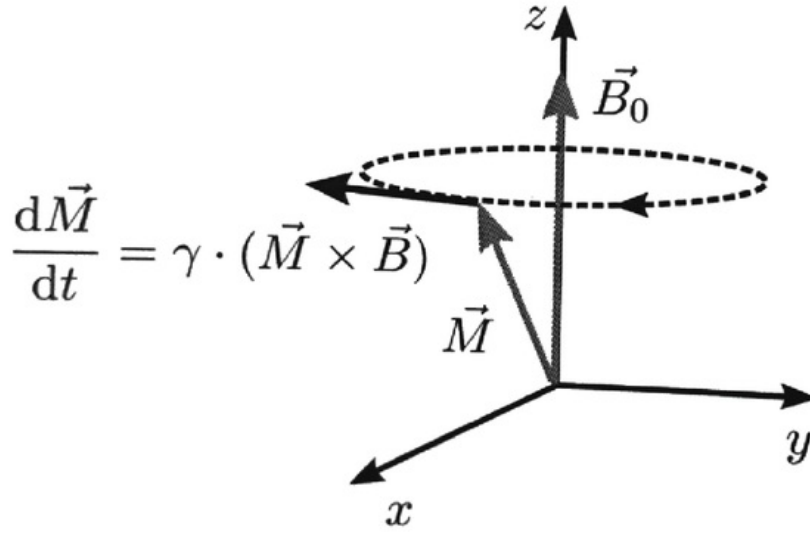


Figure 2.4: Magnetisation orientation [8].

The solution for the magnetisation is thus:

$$M_x(t) = M_x(0)\cos(\omega_L t) + M_y(0)\sin(\omega_L t) \quad (2.10)$$

$$M_y(t) = M_y(0)\cos(\omega_L t) + M_x(0)\sin(\omega_L t) \quad (2.11)$$

$$M_z(t) = M_z(0) \quad (2.12)$$

The equations describe the precessional movement of the magnetisation, M , around the direction of the magnetic field, B_0 as illustrated in Fig. 2.4. The angular frequency, or otherwise known as the Larmor frequency is expressed as:

$$\omega_L = \gamma B_0 \quad (2.13)$$

When a time varying magnetic field, B_1 , which is perpendicular to B_0 and oscillating at ω_L , is superimposed to B_0 the solution of Eq. 2.6 proves that the magnetisation M precesses simultaneously around both B_0 at ω_L and B_1 at $\omega_1 = \gamma B_1$. In a static frame of reference with respect to B_0 , when B_1 is applied it causes the magnetisation to rotate spirally down on the surface of the sphere, as in Fig. 2.5(a). Whereas when considering a frame of reference that is rotating at ω_L with the magnetisation and the rotating field B_1 , it becomes apparent that the magnetisation is rotated in a perpendicular direction to B_1 at an angular frequency ω_1 , as in Fig. 2.5(b). Therefore when an RF pulse of a certain duration t , at an angular frequency at ω_L , the magnetisation will be rotated at an angle $\alpha = \gamma B_1 t$ as is shown in Fig. 2.5(b). A RF pulse which rotates the magnetisation over an angle of $\alpha = 90^\circ$ is referred to as a 90° pulse. RF pulses are mostly characterised by their flip angle, for example 90° in this case.

[7]

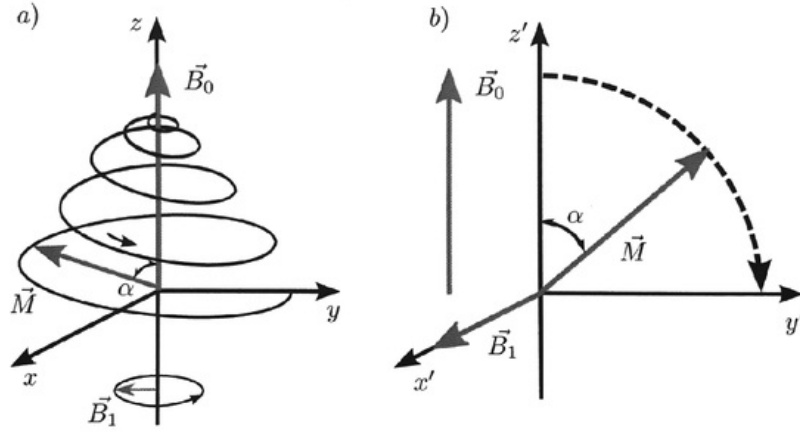


Figure 2.5: Spin orientation [8].

As the magnetisation rotates it will move away from its equilibrium and gradually it will

return to the equilibrium state being aligned with the external magnetic field, B_0 . This process is demonstrated in Eq. 2.6. The components of the magnetisation, M parallel and perpendicular to the magnetic field relax to their respective equilibrium states (M_0 and 0) at a rate that is proportional to the respective deviations from the equilibrium.

$$\frac{dM_z}{dt} = \frac{M_0 - M_z}{T_1} \quad (2.14)$$

$$\frac{dM_{x,y}}{dt} = \gamma \cdot (M \times B_0)_{x,y} - \frac{M_{x,y}}{T_2} \quad (2.15)$$

With M_0 being the equilibrium magnetisation along B_0 , T_1 the time constant whose magnetisation along B_0 is restored and T_2 representing the time constant in which the transverse component decays. Eq. 2.6, 2.14 and 2.15 collectively are known as the extended Bloch equations. When the Bloch equations are solved for a magnetisation vector, M after a 90° pulse is applied in the presence of T_1 and T_2 relaxation, it results in:

$$M_x(t) = M_0 \sin(\omega_L t) e^{-t/T_2} \quad (2.16)$$

$$M_y(t) = M_0 \cos(\omega_L t) e^{-t/T_2} \quad (2.17)$$

$$M_z(t) = M_0 (1 - e^{-t/T_1}) \quad (2.18)$$

In the static frame of reference, the longitudinal magnetisation that is along B_0 eventually will relax exponentially towards the equilibrium magnetisation M_0 while the transverse relaxation that is perpendicular to B_0 demonstrates an inward spiral movement with exponentially decreasing radius $M_0 e^{-t/T_2}$.

2.3.3 Relaxation times

Relaxation is the primary mechanism for image contrast in MRI. It can be defined as the process in which protons release the energy they absorbed from the radio frequency pulse. As resonance absorption takes place, RF energy is absorbed by the protons only when it is broadcasted at the correct frequency. All the excess energy disrupts the equilibrium arrangement of parallel and antiparallel spins to the magnetic field. Soon after this process, i.e. excitation, the protons release additional energy and return to their initial configuration by means of relaxation.

Each individual proton absorbs energy; however, relaxation times are measured for the overall entire sample as averaged results. There are two relaxation times that can be measured i.e., T_1 and T_2 relaxation time. Both relaxation times measure the spontaneous energy transfer that happens in an excited proton but vary in their final disposition of the energy. The longitudinal relaxation of the spin magnetisation vector in the presence of a static magnetic field, B_0 , is the result of a number of physical processes that occur. Primarily involving the redistribution of the nuclear spin states so that they may attain thermal equilibrium distribution, as is described by Eq. 2.4. As a result the reciprocal of the longitudinal relaxation time $\frac{1}{T_1}$ is related to the transition probability between the two energy states.

The energy that is released during these transitions will naturally transfer to the surroundings, i.e. the lattice, in the form of molecular vibrations known as phonons. Hence, this is why the longitudinal relaxation time, T_1 is also referred to as the spin-lattice relaxation which is describing the interactions in crystal lattices. As the longitudinal relaxation leads to thermal equilibrium, it results in the increase of the entropy of the spin system.

Transverse magnetisation decay is a result of a loss of phase coherence of precessing spins. As the local magnetic field fluctuates randomly it causes variations in the immediate Larmor frequency of the different spins. As a result, the coherent spin precession movement will dephase. Then as a consequence, the net magnetisation of a spin ensemble will decrease [7]. The local magnetic field inhomogeneities which cause spin dephasing subdivide into two magnitude levels. One of the levels is responsible for grouping the rapidly fluctuating magnetic field inhomogeneities which are a result of the moving electrons and nuclei. These fluctuating magnetic field inhomogeneities cause an irreversible process of transverse relaxation or otherwise known as T_2 decay or spin-spin relaxation.

The other level of inhomogeneities is responsible for the static magnetic inhomogeneities that are related to the heterogeneous tissue structures. Heterogeneous tissues have distinct magnetic susceptibilities and consequently cause microscopic field inhomogeneities that are larger than the size of a spin ensemble. These static inhomogeneities are the cause of the reversible process of transverse relaxation or better known as T_2^* decay. In the study of transverse relaxation, mainly T_2^* relaxation time is studied [7].

T_1 and T_2 relaxation times are both dependent on the magnetic field strength, although its effect being more dominant on T_1 relaxation time as compared to its effect on T_2 relaxation time. In a given sample it is a known fact that the T_1 relaxation time of spins is nearly always longer than the T_2 relaxation time of spins. Relaxation is commonly expressed in terms of relaxation rates, i.e. R_1 and R_2 as opposed to relaxation times ($R_1 = \frac{1}{T_1}$ and $R_2 = \frac{1}{T_2}$).

The precessing transverse magnetisation is detected when an electrical conduction coil surrounds the subject in the transverse plane. The rotating magnetisation consequently induces a voltage in the coil. What will be shown is that the voltage amplitude will

undergo T_2^* relaxation as it decays exponentially. This phenomenon is more precisely known as Free Induction Decay (FID), which is essentially the signal studied in an NMR experiment (as shown in Fig. 2.6 below). [7]

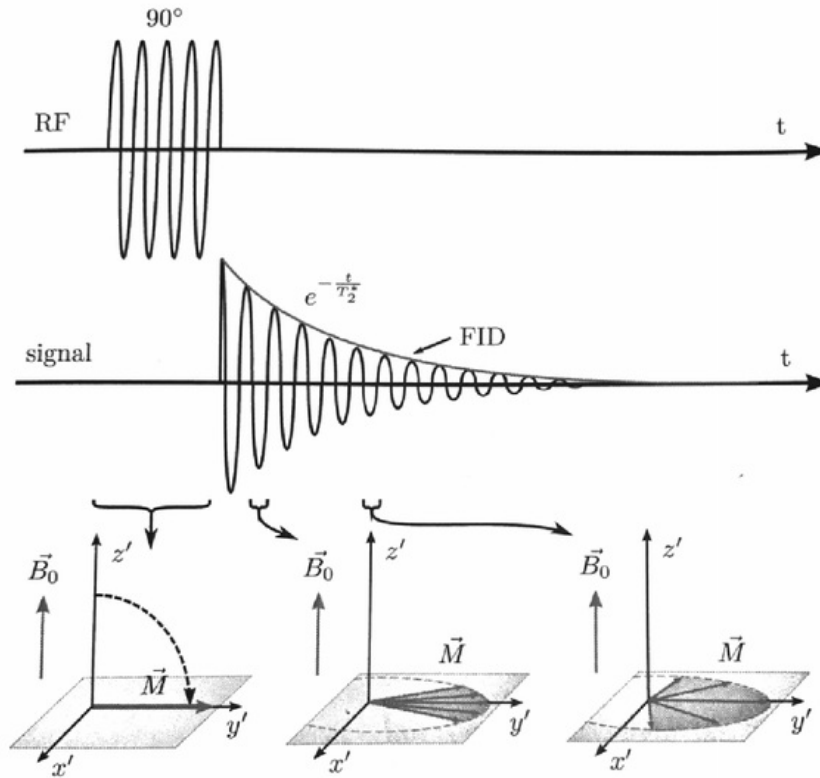


Figure 2.6: Transverse relaxation [7]

Fig. 2.6 illustrates how after an RF pulse is applied, the voltage amplitude of the NMR signal decays exponentially. The reason being the process of transverse relaxation taking place which has a time constant of T_2^* . The graphs below depict the nuclear magnetic dipole moments which dephase during precession as is depicted in a rotating frame of reference.

The uniqueness of NMR experiments is in the fact that it not only takes into account relaxation times (T_1 and T_2) but also the proton density and diffusion properties which are different for various tissue types and pathological states, as is shown in Table 2 below.

Table 2.2: T_1 and T_2 relaxation times for various biological tissue at a magnetic field of 1.5T [7]

Tissue type	T_1 (ms)	T_2 (ms)
Brain white matter	790	90
Brain gray matter	920	100
Blood	1200	50
Lung	830	80
Myocardium	870	60
Skeletal muscle	870	50
Lipids	260	80

Therefore because of this contrast generated in relaxation processes, it allows for clinically specific images to be obtained. Contrast weighted images of the NMR signal can be acquired by the creation of pulse sequences that consist of repetitive blocks of RF pulses. The upcoming sections will further discuss various pulse sequences in depth.

2.3.4 Transverse relaxation time

The transverse relaxation time or T_2 relaxation time (also referred to as spin-spin relaxation time) can be defined as the time that is required for the spinning protons to lose phase coherence with the nuclei that are spinning perpendicular to the main magnetic field. The time for decay is measured until about 37% of its initial value has decayed. This process occurs as a consequence of interactions between various spins which results in a reduction in transverse magnetisation.

The mechanism that is used for measuring the transverse relaxation time weighting of the signal is called the spin-echo. Recalling that M_0 is oriented along the z axis at equilibrium and there is no part of M_0 that is situated on the xy axis. The coherence, as we call it, is completely longitudinal. When an RF pulse at a 90° angle is applied the energy that is absorbed causes M_0 to rotate completely into the xy plane. Consequently, the coherence becomes situated in the transverse plane towards the end of the plane, as is shown in Fig. 2.7 below.

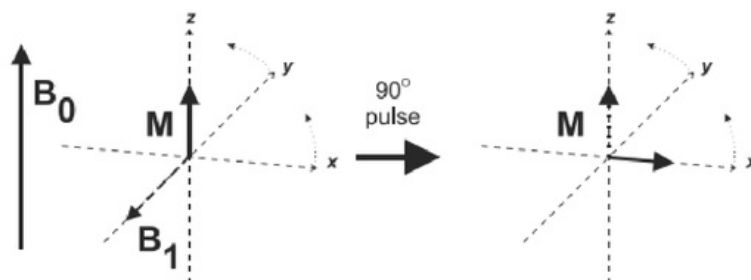


Figure 2.7: Orientation after RF pulse [15].

During this time a few processes take place, such as the coherence eventually disappears and the protons release their energy and reorient themselves with B_0 . As a result of the coherence disappearing, it gives rise to the FID signal which quickly decays because of the strong T_2^* dephasing of the spin coherence. Additionally it causes the value of M to decrease to 0. In other words, T_2 relaxation is the process in which transverse magnetisation is lost.

Analysing further in depth by observing the macroscopic diagram (as in Fig. 2.7) provides a thorough understanding. Towards the end of the applied 90° RF pulse, after the protons have absorbed the energy and have oriented themselves along the transverse plane, each proton begins to precess at the mutual frequency of ω_0 and is synchronised at the same phase of its precessional cycle. Neighbouring protons of the same type which have the same molecular environment are also subjected to an equal ω_0 . Consequently the protons can almost instantly absorb the energy that is being emitted by the neighbouring protons. This process is otherwise known as spin-spin relaxation which describes the energy transfer from an excited proton to a neighbour proton. The energy that is absorbed remains as spin excitation as opposed to being transferred to the surroundings (in the case of T_1). Spin-spin relaxation can occur several times provided that the two conditions are met, i.e. the protons remain with close proximity and the protons remain at the same ω_0 .

Intermolecular as well as intramolecular interactions are the reason for the fluctuations of ω_0 . The outcome of this fluctuation is a gradual and permanent loss of phase coherence to the spins as energy exchange occurs and consequently reduces the magnitude of the transverse magnetisation and the generated signal. T_2 relaxation is precisely when the transverse magnetisation is 37% of its initial value, immediately after the 90° RF pulse is applied. Eventually as already mentioned, the transverse coherence disappears entirely as it reorients into the longitudinal direction as T_1 relaxation occurs. It is a known fact that the T_2 dephasing time is always less than or equal to the T_1 dephasing time.

However, if after the 90° RF pulse a 180° RF pulse follows at the time $TE/2$ (as in Fig. 2.8) then the spins become flipped in orientation by the 180° pulse and rephase themselves to produce a signal that is measureable (S) at the echo time TE and S_0 which constitutes the signal strength after the initial 90° pulse.

$$S = S_0 e^{-\frac{TE}{T_2}} \quad (2.19)$$

Spin dephasing that occurs as a result of large static magnetic field inhomogeneities is counteracted by flipping the spins by 180° by means of refocusing (180°) pulse. In comparison to spin dephasing that occurs by local, rapidly fluctuating magnetic field inhomogeneities which is not rephased. Therefore, the spin echo signal, as in Eq. 2.19, is weighted by the transverse relaxation time T_2 .

A way to determine T_2 is by repeating the spin echo experiment multiple times with different TE values and substituting those results into Eq. 2.19. Although it is necessary to ensure that the repetition time, TR , between the experiment should be sufficient to allow full magnetisation recovery. This method produces a reasonable and acceptable estimate of T_2 however, Eq. 2.19 is only valid when a few relaxation mechanisms are disregarded.

The other method to measure T_2 is by multi spin echo sequence in which a 90° pulse is then followed by a block of uniformly spaced 180° pulses. The result is that in between each pair of 180° pulses that are separated by a time TE , a spin echo will appear. The signal that appears after every subsequent echo, i, decays with T_2 . [7]

$$S = S_0 e^{-i\frac{TE}{T_2}} \quad (2.20)$$

2.3.5 Longitudinal relaxation time

Longitudinal relaxation or T_1 relaxation time is essentially the time that is required for the z component of M , to return to approximately 67% of its initial value after being subjected to an excitation RF pulse.

Recalling from earlier that M_0 is parallel to B_0 when at equilibrium, then when energy absorption occurs it will rotate M_0 into the transverse plane. It is actually T_1 relaxation that helps enable this process. T_1 relaxation aids protons to give away their energy so that they may return to their initial orientation. When a 90° RF pulse is applied, M_0 will rotate and this results in there being no longitudinal magnetisation being present at the end of the pulse. Gradually the longitudinal magnetisation returns because of the protons that

release energy. As the longitudinal magnetisation returns it creates an exponential growth with T_1 acting as the time constant in the following equation to describe the rate of growth:

$$M(\tau) = M_0(1 - e^{-\frac{\tau}{T_1}}) \quad (2.21)$$

Where τ represents the time following the RF pulse. After three T_1 time periods have occurred it results in M having 95% returned to its initial value it was before the excitation pulse, M_0 . Therefore, this is reason why T_1 relaxation time is also referred to as spin-lattice relaxation. The term spin-lattice refers to the notion that the excited proton (or the spin) transfers its energy to its surroundings (or the lattice) as opposed to another spin. The energy does not play any further part in the spin excitation.

As previously stated in the spin echo description (in reference to Eq. 2.19) that it is only valid when the TR between the repetition experiments should be sufficient to allow full magnetisation recovery. If this condition is not met it then becomes that signal intensity in a spin echo is function of both the echo time TE and the repetition time, TR. This is represented by the following Eq. 2.22.

$$S(\tau) = S_0(1 - e^{-\frac{TR}{T_1}})e^{-\frac{TE}{T_2}} \quad (2.22)$$

T_1 relaxation can be measured by means of the inversion recovery sequence. In the process the first RF pulse in the sequence is a 180° pulse that is inverted. This pulse plays the role of inverting the magnetisation and after it has done that it will restore itself to the equilibrium state by T_1 relaxation at an inversion time, TI.

After TI is complete the magnetisation is rotated in the transverse plane through a 90° pulse. The result is a signal that is proportional to the longitudinal magnetisation right before the 90° pulse. The z-component of the magnetisation recovers exponentially according to the following Eq. 2.2.

$$M_z = M_0(1 - (1 - \cos\theta_{inv})e^{-\frac{TI}{T_1}} + e^{-\frac{TE}{T_2}}) \quad (2.23)$$

Where θ_{inv} constitutes the flip angle of the inversion pulse. With a handful of images that have an appropriate range of inversion times, they can be used to quantitatively fit T_1 relaxation times. Another technique which has the similar concept to the inversion

recovery sequence is the saturation recovery sequence. The only difference is that 180° inversion pulse is substituted by a 90° pulse, which is then followed by spoiler gradient. A point to take note of is that when Eq. 2.24, the equation for the inversion recovery sequence, equates to zero when the inversion time is:

$$TI_{null} = T_1 [\ln 2 - \ln(1 + e^{-\frac{TR}{T_1}})] \quad (2.24)$$

This is an important property that is made use of when one is trying to suppress or accentuate tissues that have a specific T_1 .

In conclusion the crucial difference between T_1 and T_2 relaxation is in the degree of influence of B_0 . T_1 is very sensitive to B_0 , with longer T_1 times measured for a tissue at higher B_0 . T_2 is comparatively insensitive to B_0 at relatively large magnetic field strengths that are currently used in MRI. The only significant changes in T_2 occur when there is very low B_0 , such as less than 0.05 T.

2.4 Quantitative Magnetic Resonance Imaging

In the present day MRI has become the widely accepted clinical imaging process for the visualisation of complex internal structures. The process produces MR images, i.e. qualitative data, which is then comprehended by a skilled person in the field. These qualitative images illustrate a combination of parameters such as the relaxation parameters of the body, as well as machine parameters like flip angle, gain and image scaling.

For the purpose of most diagnostics this level of imaging is sufficient but if further detailed study is required this level becomes insufficient and quantitative analysis becomes a necessity. Quantitative MRI would allow for things such as biological changes in diseases and the natural response of the body from treatments to be quantified.

Quantitative MRI begins from a process of acquiring pictures where the skilled observer will comprehend the dark, light, large and small objects into real physical objects and will thereafter translate these findings into a measurement process, as is traditionally done with scientific experimentation results. In this way, it becomes possible to measure a vast range of quantities, to test varying ranges and to monitor changes from a previous image. Therefore, MR scanners when used as a tool for measurement of quantities that are clinically relevant have opened a wide range of scopes and possibilities. Images that are quantitative illustrate any discrepancies against the normal ranges, changes from previous images and possible image interpretations. An example of this are diseased areas which have diffused and there are no clear boundaries of its area are difficult to detect when observed qualitatively however, when they are quantitatively studied they are able to be studied in depth.

As MRIs become shifted from the standard qualitative image to more detailed images encapsulating the measurements of parameters, the images become substituted by quantitative parameter maps, as is shown in Fig. 2.8. The quantitative parametric maps appear identical to images but the major difference and the notion which separates the two is that in the quantitative parameter maps each pixel is represented by a numeric value as compared to the signal intensity being represented by an arbitrary scale. [7]

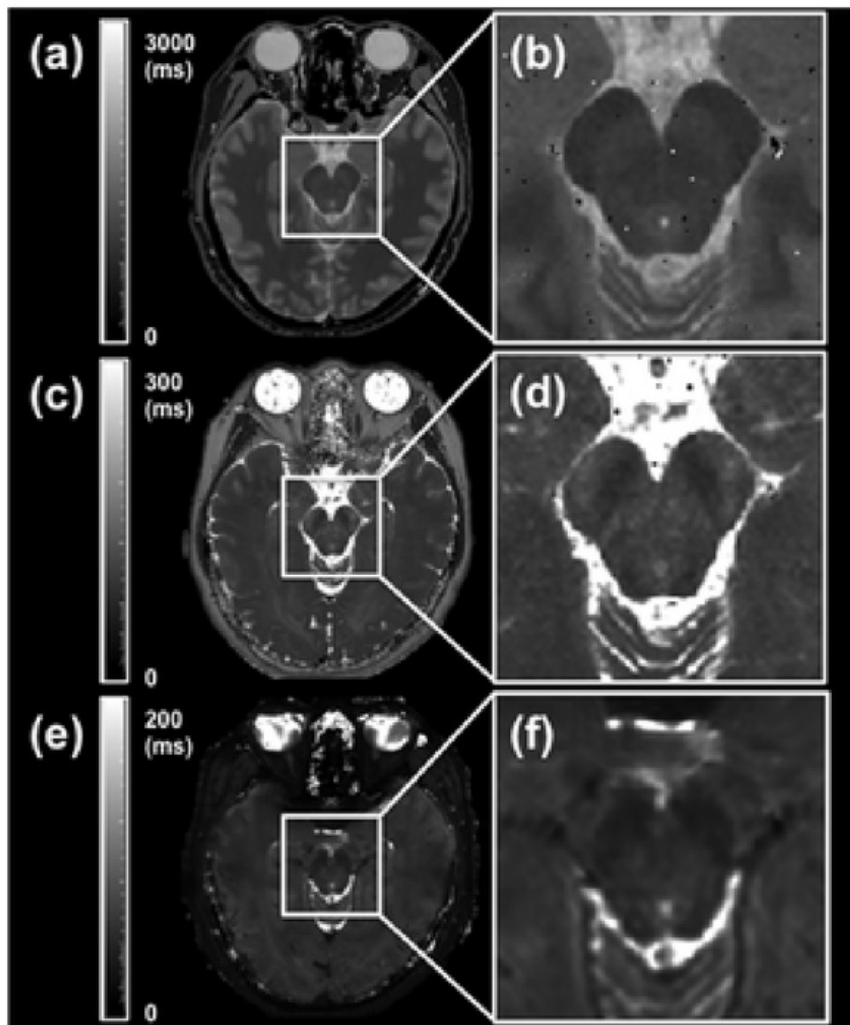


Figure 2.8: Quantitative T_1 , T_2 , and T_2^* maps of the lower midbrain. [21].

Fig. 2.8 shows the quantitative T_1 AND T_2 maps of a transverse slice of a patients head. In the image each pixel has a number it corresponds to which is translated by the colour bars on the right of each image (a-d).

2.5 Multi-nuclear MRI

In standard MRI, ^1H , hydrogen protons are mainly used for the purpose of imaging. However as was mentioned in Table 1, other nuclei also have the capability to be used in MRI and used in the same imaging techniques as hydrogen protons are. Some useful nuclei include, Phosphorous-31 and Sodium-23, which are naturally occurring within living organisms. It is possible to also combine some nuclei with suitable molecules and administer to patients which is soon followed by an MRI and MRS to study targeted areas. Additionally nuclei such as Helium-3, Xenon-129 and Carbon-13 that are magnetised can be even further magnetised through means of hyperpolarisation techniques in order to strengthen the MRI signal and hence obtain higher resolution images.

Therefore it has become evident in the recent years the huge scope that multinuclear MRI presents to the medical imaging field. Many methods are already in use and others are continually being discovered and trialled. Each method is an entire research domain on its own. A brief overview of some potential nuclei that can be used in multinuclear MRI is described below.

2.5.1 Fluorine-19 (^{19}F)

Fluorine is naturally present in the human body, such as in bones and teeth, but in very low concentrations. This means that endogenous fluorine has comparatively short T_2 relaxation times as opposed to exogenous administered fluorine compounds (with negligible background).

Additionally ^{19}F is 100 abundant isotopically and its gyromagnetic ratio is very similar to hydrogen-1 with a relative sensitivity of 83.2% compared to hydrogen-1. Another fact is that ^{19}F NMR chemical shift is sensitive to disturbances in the chemical micro-environment. ^{19}F nuclei are active reporter molecules that are used to indicate pH levels, and presence of metal ions such as Mg^{2+} , Ca^{2+} and Na^{2+} , which ^{19}F is capable of detecting as it is highly sensitive to chemical shift changes. Fluorine-19 also detects hypoxia as well as tissue oxygenation. Hypoxia is indicated due to the formation of retained bioreduction products from administered nitroimidazoles in hypoxic conditions [7].

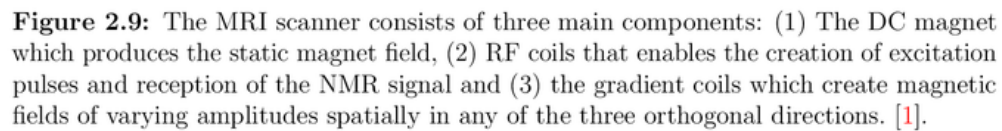
Tissue oxygenation is measured by using perfluorocarbon compounds, which act as oxygenation markers. Perfluorocarbons are simply hydrocarbons whose hydrogen atoms have been substituted by fluorine atoms. The result is that the transverse relaxation rate, R_1 of these perfluorocarbons happens to increase linearly with the dissolved oxygen

concentrations. With the linear relation that is established it then becomes possible to quantitatively measure interstitial oxygen concentrations [7]. This notion will be further discussed in detail in chapter 4.

2.6 MRI hardware

Medical MRI scanners are used for the routine patient examinations. The MRI scanners are situated inside an RF shielded room so that the MR signal can be free of interference from other RF transmitters. The fundamental components of MRI scanners are essentially, a superconducting magnet which serves the purpose of generating the B_0 field, shim coils which are responsible for maintaining the B_0 homogeneity, gradient coils which are the key in producing imaging gradients and radio frequency coils that are solely responsible for the B_1 field transmission and reception.

There are also additional attachable RF coils that are available for use for certain anatomies. The major advantage of the RF coils is that they are specifically tuned to the Larmor frequency of the nucleus that is to be imaged.



Chapter 3

Literature Review: Cancer, hypoxia and oximetry

3.1 Overview

In living organisms, specifically multicellular organisms the amount of cells that are within the organism are regulated by the bodily process of cell division and self-elimination. Other mechanisms within the body control cell differentiation state, monitor and maintain tissue integrity by limiting cells to stay within their tissue boundaries. However, when genetic mutations arise cells are free to escape these control mechanisms and boundaries. This results in the process of cell self-annihilation collapsing and an uncontrollable process of cell division occurring leading to cancer [7].

Additionally, when cancer arises the cancer cells become variant to normal cells in cell structure and anatomy. They tend to survive outside tissue boundaries which can lead to further problems like metastasis.

The purpose of this chapter is to give a brief summary of cancer formation, oncogenesis, cancer epidemiology and cancer treatment. An emphasis is on the cancer treatment technique of radiotherapy with focus on the possibilities of combining quantitative tumour parameter maps into a biologically aided radiotherapy. The next section follows a detailed discussion of hypoxia, its origins, effects and the consequences it poses for cancer treatment. Lastly the chapter elaborates on current techniques that are used for tumour oximetry.

3.2 Oncogenesis

Cancer is a result of a malignant growth of a tumour. There are several stages cells undergo, prior to reaching malignancy. Each of these stages comprise of rapid cell division which lead to the inhibition of normal cell mechanisms, this in turn controls the outcome of cell proliferation. As healthy cells are transformed to cancer cells there are genetic mutations in three specific groups of genes that are of particular interest.

Two groups of genes are the proto-oncogenes and tumour suppressor genes, which are collectively responsible for the synthesis of signalling those molecules that regulate cell growth. When there is an increase in the signaling for the growth promoting gene it results in an excess cell growth as a result of the incompetence to respond to the extra cellular growth suppressing signals. Normally, the excess growth would be monitored and kept within limits by the action of tumour suppressor genes whose role is to decrease cell growth. However, in the case of cancer these tumour suppressor genes remain inactive and allow the proliferation of genetic mutations.

The third group of genes which are affected by genetic mutations are the DNA stability genes or caretaker genes, their role is to maintain and preserve the properties and characteristics of DNA. When genetic mutations occur in this gene the immediate course of action is not cell division, but rather decreasing the stability. This happens as a result of inhibiting the proper repair of damaged DNA. Consequently, the damaged DNA becomes a part of a cycle of genetic mutations. [7].

The causes of genetic mutations are vast but can be largely due to carcinogenic agents such as chemicals like asbestos, exposure to ionizing radiation and biological agents such as hepatitis B and C.

In the initial stages of cancer, genes of the three groups mentioned above are altered. These genes are essential in two main areas: for the preservation of the integrity of the genome and the regulation and growth of cells. When these processes are tampered with the consequences are rapidly dividing cells that contain gene mutations in the gene groups that are linked with cancer. As proliferation of mutations in cancer-linked genes increases, the tumour continues to flourish until gradually it begins to invade neighbouring tissues and organs or otherwise known as metastasis. [7]

3.3 Cancer epidemiology

Cancer is one of the main causes of death worldwide and is responsible for 8.8 million deaths that occurred in 2015 [3]. On a global scale, 1 in every 6 deaths are due to cancer. In 2013 there were 124465 new cases of cancer diagnosed in Australia [24]. Of the 124465 new cases, 68936 were males and the remainder females.

Cancer type	New cases 2017	% of all new cancers 2017
Breast	17730	13.2
Breast (among females)	17586	28.4
Colorectal	16682	12.4
Prostate	16665	23.1
Melanoma	13941	10.4
Lung	12434	9.3

Table 3.1: The table shows the estimated most common cancers diagnosed in 2017 in Australia. [24]

In contrast, for 2017 the estimated most frequent causes of death by cancer in Australia are lung (18.9%), breast (among females, 14.9%), prostate (12.7%), colorectal (8.6%), breast (6.5%) and pancreatic (6.1%).

However, between the years of 1984-1988 and 2009-2013 the five-year relative survival from all cancers combined improved from 48% to 68%. The increase in cancer survival can be credited to the constant improvements in cancer diagnosis and appropriate therapy.

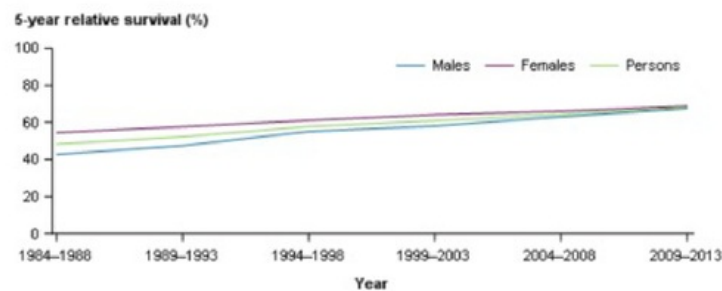


Figure 3.1: 5-year relative survival from all cancers combined, by sex, 1984-1988 to 2009-2013 [24]

Nearly 30-50% of cancers can currently be prevented by avoiding risk factors such as tobacco use, obesity, poor nutrition, physical inactivity, heavy use of alcohol and infectious agents such as hepatitis B and human papilloma virus (HPV). All of the risk factors mentioned are preventable by simple behavioural changes and vaccines. Additionally, individuals have high chances of being cured if they are diagnosed early and treated adequately.

3.4 Cancer treatment

The treatment of cancer is subject to various factors which need to be taken into account for. These factors include things like the nature of the tumour, its anatomical location in the body, the severity or clinical stage of the tumour and the general health of the patient. This is known as a multidisciplinary approach and is generally a combination of the three main cancer treatment mediums, i.e. surgery, chemotherapy and radiotherapy and is therefore a cooperation of several clinical departments.

Surgery aims to completely remove the tumour tissue. However, since tumours have the capability to become invasive to neighbouring tissue it is quite possible that remnants of the tumour tissue would be left behind and thus a wider surgical margin has to be taken into consideration. Also, if there are lymph nodes present in the tumour area they may be removed in order to test for and if possible prevent the spread of metastatic cells.

The impact of surgery is local whereas chemotherapy is a systemic treatment, i.e. it affects the whole body. Chemotherapy involves the administration of chemical and organic molecules which kill all the rapidly dividing cells in the human body regardless of the nature of the cell. This means that not only are rapidly dividing tumour cells directly targeted by chemotherapy but so are the other fast dividing cells such as hair follicles, skin and gastrointestinal cells. In order to reduce the side effects of the drugs the optimal combination of chemotherapeutic drugs comprises of the original chemotherapeutics (which possess the ability to kill dividing cells), in combination with newer hormonal treatments (which are molecules that are designed to target a specific process in the tumour cell) and lastly treatments designed to increase the activity of the host towards the tumour (immunotherapy, vaccines) [11] [18].

Radiotherapy utilises ionising radiation for the purpose of damaging tumour cells. The ionising radiation comes from either a linear accelerator or radioactive sources. The most frequently used and common form of radiotherapy is external beam radiotherapy. External beam radiotherapy focuses on outputting radiation doses into malignant tumour tissue. The radiation doses aim to be highly uniform and also preserve the neighbouring healthy tissue in the body. The original radiotherapy treatment that was developed fired radiation beams of either square or rectangle shapes at various angles. However, because the shape of tumours are irregular this kind of treatment was not highly effective.

Therefore, modern radiotherapy treatments are specific and closely matched to individual tumours. This is achieved by using three dimensional medical imaging techniques such as MRI, CT and PET images which display the targeted tumour area and volume as well as surrounding normal functioning organs. In this way the data from three dimensional planning images aids in the determination of the specific type of radiation beam orientation and shapes resulting in a tailored three dimensional dose distribution for a patient.

An important development in radiotherapy was the Multi-Leaf Collimator (MLC). The

multi-leaf collimator produces radiation beams that match the irregular shape of the tumour tissue. A more advanced radiotherapy technique is Intensity Modulated Radiation Therapy (IMRT) and is used to minimise the amount of healthy tissue being irradiated by radiotherapy treatment. It is achieved by moving the leaves of the MLC in the duration of the treatment. By doing so the several beam segments end up being superimposed on top of each other allowing the radiation dose to be varied in intensity in the specific beam direction required. A higher level of radiation beam modulation is acquired when the shape of the radiation beam is constantly adapted during an arc motion of the gantry of the linear accelerator around the patient, known as Intensity Modulated Arc Therapy (IMAT).

Another advanced radiation therapy is Image-Guided Radiation Therapy (IGRT). IGRT takes into consideration the changes that occur in the position of the tumour and its orientation in between treatment sessions. The current developments in radiotherapy aim to integrate tumour parameters in the radiation dose planning which is known as Biologically Guided Radiotherapy (BGRT). With tumour parameter maps a specific and more effective radiation dose is delivered to the patient that is aligned to the radiation sensitivity and the malignancy of the tumour.

When the human body is exposed to ionising radiation by radiotherapy the immediate effect of radiation in the body is observed in the physical interaction between radiation and on the molecules of cells. The most critical damage done by radiation is on the crucial elements of the cell for e.g. DNA. Damage to other crucial cell areas can also lead to cell death. When ionising radiation interacts directly with crucial elements of a cell it causes it to become excited or ionised by Coulomb interactions. Ionising radiation also cause damage in the body by their interaction with other atoms to form free radicals, such as H_2O^+ and OH . The free radicals are very reactive molecules because of their atomic structure in which they have an unpaired valence electron. The free radicals are capable of damaging the crucial cell organelles by means of diffusing into key areas. This kind of indirect damage by ionising radiation is accountable for nearly two thirds of the damage by biological radiation.

3.5 Hypoxia

Hypoxia can be defined as the condition in which the body or areas of the body are lacking in an adequate supply of oxygen at the tissue level. The condition is not common in normal functioning tissue but frequently appears in tumours and is often described as a characteristic feature of tumours.

The work of Thomlinson and Gray in the 1950s highlighted the effect oxygen had on the radiation response in various microbial, cellular, animal and plant model systems. Thomlinson and Gray were the first to produce evidence of hypoxia in tumours through their study of human lung cancer. Their mathematical modelling of the delivery of oxygen,

oxygen consumption and the regional oxygen distribution within the tumours lead to the suggestion that the tumours had areas where viable cells were being placed in chronic and severe hypoxic conditions. Another observation they made was of necrosis in the central section of lung cancers surrounded by vasculature. They noticed that the thickness of the resulting viable shell of tissue situated at the exterior of the tissue was measured to be 100-180 μm , which is similar to the distance where the process of diffusion and consumption of oxygen take place in respiring bodily tissues and are balanced. Therefore, they came to the conclusion that upper cell layers of the tumour tissue consumed the most of the oxygen supplied by exterior blood vessels which resulted in the inner cell mass to be deprived of oxygen [7].

Over time, there have been numerous critical oxygen partial pressures for hypoxia defined with respect to the cellular/subcellular or molecular mechanisms under study [13]. Due to oxygen partial pressure thresholds used in different applications differing there is no single, standard hypoxic threshold that is generally applicable. Since the initial observation of tumour hypoxia much research has been invested into the clarification and thorough understanding of its role in tumour biology and how it affects treatment. The following sections summarise the most important aspects of hypoxia. [20] [16] [23]. More information about hypoxia can be read in the Appendix A.

3.5.1 Origin of hypoxia

The oxygen concentration in a tissue has two main contributing factors: oxygen supply and oxygen consumption. It is not simply the local oxygen consumption that is indicative of the final oxygen concentration but also the consumption of oxygen of all the surrounding cells that separate a particular cell from the nearest blood vessel that is supplying oxygen. Additionally, the oxygen pressure, pO_2 of the closest blood vessel is measured by the oxygen consumption of the tissues upstream the vascular tree and by arterial input pO_2 . Hypoxia is not confined to only tumours; healthy tissue can also experience low pO_2 for various reasons. These reasons are for example, low arterial input pO_2 (for e.g. pulmonary diseases), a reduced oxygen carrying capability of the blood (for e.g. by anaemia), local or entire reduction in tissue perfusion or increased oxygen diffusion distances because of the distortion to the diffusion geometry [13]. When there is low oxygen concentration in normal, healthy tissues a signal activates the regulatory processes in the body that will compensate the oxygen shortages by increasing the blood stream or decreasing the oxygen utilisation. This however is not the case in tumour hypoxia as tumour tissue is not capable to efficiently counteract the decrease in oxygen levels.

Approximately 90% of nearly all cancers are comprised of solid tumour masses [23]. Solid tumours arise from a single cell that has mutated. The tumour progresses rapidly, initially by proliferating in a certain region, followed by local invasion into healthy neighbouring tissue and eventually distant metastasis. The rapid cellular growth of the tumour occurs because of the alterations in the structure and microenvironment of the tumour cells. Mainly the alterations are credited to the inadequate supply of oxygen which results in the eventual hypoxic and even anoxic conditions.

As tumours grow rapidly they also outgrow the oxygen supplying capacity of its original vascular network. As a result, the growing tumours develop their own vascular networks and blood supply. This is achieved by incorporating neighbouring host vessels or by forming entirely new micro vessels by means of tumour angiogenesis factors [23]. These newly formed vascular networks are very different to the vascular networks that are found in healthy tissue, they generally display a wide range of functional and structural abnormalities. These include things such as dilations, absent or incomplete endothelial linings and basement membranes, leakiness, irregular and tortuous architecture, blind ends and others. The consequence of these abnormalities is that the flow of blood becomes irregular and sluggish and therefore diminishes the delivery of oxygen to tumour cells and as a result leads to hypoxic and even anoxic conditions in regions. The oxygenation status in a tumour can become worse when diffusion distances increase. This happens when the tumour cells spread to a distance in which the adequate delivery of oxygen by the blood vessels is not possible.

Tumour hypoxia originates from three areas: perfusion, diffusion and anaemia related causes. Perfusion related hypoxia in tumours is caused by an inefficient blood flow in the tumour. The tumour's vascular network is disturbed by structural and functional abnormalities such as dilation, elongation, etc. Vascular networks can also be bypassed by large shunt blood vessels while some micro vessels may be too narrow to even carry red blood cells. Such mechanisms cause transient effects, therefore the condition is known as acute hypoxia.

Diffusion related hypoxia is a result of an increased oxygen diffusion distances. The tumour cells move away from perivascular areas due to proliferation pressure and cells that are located past the oxygen diffusion boundary experience an inadequate oxygen supply. The exact location of the oxygen diffusion boundary is not known as it depends on factors such as how stable or unstable the blood flow is and the varying cell oxygen consumption rates. Because the nature of diffusion tends to be long-lived the condition is referred to as chronic hypoxia. Chronic hypoxia was initially thought of as mainly related to the radial gradients of oxygen concentration with respect to the blood vessel. However it is not only the radial oxygen concentration gradients that need to be considered but also the longitudinal oxygen gradients that are along the blood vessel, which also play a major role in hypoxia. The longitudinal gradients impact various things such as the functioning of the long microvessels, low arterial blood pO_2 and the fluctuating oxygen consumption rates. Small changes in oxygen consumption rates are capable of causing large oxygen deficiencies downstream [7].

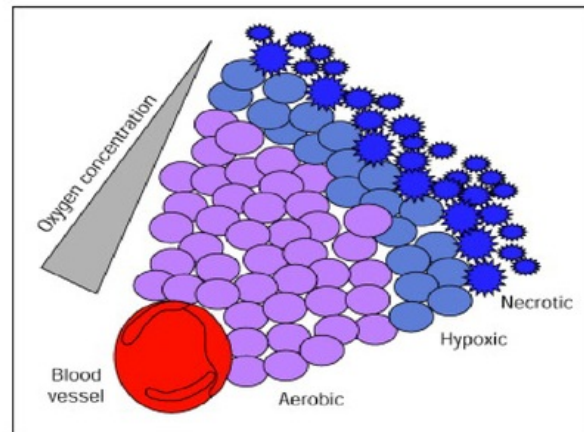


Figure 3.2: The figure illustrates the diffusion of oxygen from a capillary in to tumour tissue. Radial oxygen diffusion distances are restricted by oxygen consumption and as a result the oxygen supply becomes insufficient at greater distances. Cells become hypoxic, but still viable when oxygen concentration is low and necrotic when the oxygen concentration becomes zero. [24]

Anaemia related hypoxia happens when the oxygen transport capacity of blood decreases because of tumour-related or therapy induced effects. For example, when hypoxic cells stiffen it increases the viscosity of blood and hinders the flow of blood.

Another important feature of hypoxia is its cyclic nature. The cyclic hypoxia behaviour is a consequence of the superposition by two phenomena. The first phenomenon, is that the overall oxygenation state of large tumour regions cycles slowly having a timescale of hours to days. The slow cycles are a result of the major changes to the vascular network. In the second phenomenon cycles at a faster rate, i.e. a few times per hour as a result of the changes in the red blood cell flux of micro vessels. The faster cycle is a result of factors such as smaller vascular reconstructions (for example, blood vessels split into much smaller parallel vessels), vasodilation of downstream vessels or cells partitioning disproportionately at bifurcations. Vascular reconstruction has a greater impact than in normal tissue because hypoxic blood cells become stiffened. Therefore because of cyclic hypoxia, comparatively large regions can experience transient periods of hypoxia and re-oxygenation [7].

3.5.2 Effects of hypoxia

In tumours, hypoxia has the capability to act as a stressor whereby it impairs cell growth and can potentially cause cell death. It can also drive the tumour to the malignancy stage and increase its resistance to therapies. Malignancy and increased resistance to therapies is credited to hypoxia-induced proteomic and genomic changes that occur in the tumour cells.

When the partial pressure of oxygen drops to a value lower than 10mmHg in tumour cells it causes the cells to increase the expression of several genes, which therefore changes the proteomic content of the tumour cell. The hypoxia-inducible transcription factor (HIF-1) is responsible for the increased expression of genes. HIF-1 is comprised of two subcomponents, HIF-1 α and HIF-1 β . HIF-1 β is existing in cells regardless of the oxygenation status, whereas HIF-1 α is directly degraded when exposed to atmospheric oxygen. However when HIF-1 α is subjected to hypoxic conditions it is no longer degraded. As a result in hypoxic conditions HIF-1 and HIF-1 β heterodimerise. Thereafter HIF-1 dimers bind to DNA at hypoxia response elements in order to upregulate the transcription of specific genes. The upregulated genes produced are responsible for the increase of oxygen transport, promoting angiogenesis, and energy preservation (for example, glucose transporters). The proteomic changes are also responsible for cell apoptosis and survival.

Hypoxia is also responsible for the changes in the genome of neoplastic cells. Tumour cells that have a partial pressure of oxygen less than 1mmHg become susceptible to genetic changes such as point mutations, the amplification of genes and rearrangement of chromosomes. As the genetic mutations increase, simultaneously hypoxia exerts a selecting physiological pressure in tumours. This means that the tumour cells that are composed of genetic changes that are favourable in hypoxic conditions are selected over other cells. Therefore the Darwinian selection process of selecting the most resistant clones takes place. The consequence of this selection process is that it leads to a very aggressive form of hypoxia and eventual malignant progression because of the favourability of those neoplastic cells that have apoptotic insensitivity and an enhanced angiogenic potential.

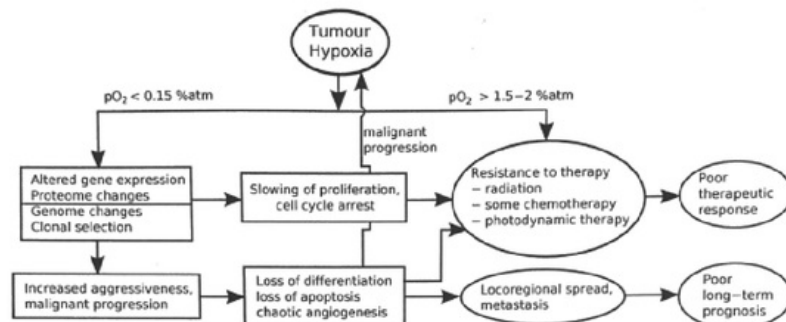


Figure 3.3: The figure shows a schematic representation of the effects of hypoxia on tumour progression and resistance to therapy [7]

3.5.3 Consequences for cancer treatment

The effects of hypoxia lead to the gradual therapy resistance and thus unfavourable disease prognosis. Consequently, hypoxia has been linked to treatment outcome and has also been shown to be a prognostic factor in the majority of head and neck cancers, soft tissue carcinoma [12], cervical cancers, brain cancers, and others. In these studies the subdivision of tumours into either oxic or hypoxic categories is based on a single threshold for median tumour pO_2 , for e.g. 5mmHg or 10mmHg respectively. Although the classification into oxic and hypoxic classes is quite broad and could be improved, it already has a significant prognostic strength. Therefore, it is expected that imaging pO_2 will further enhance prognosis and treatment of cancer.

The resistance of hypoxic tumours to therapy impacts the efficacy of the two main treatment modalities of cancer, i.e. chemotherapy and radiotherapy. Chemotherapy is disturbed because of the insufficient drug delivery due to increased diffusion distances and by the decreased efficacy of some cytotoxic drugs because of hypoxic conditions. As we know already, hypoxic cells are subject to cell cycle inhibition and decreases in growth fraction making them less vulnerable to chemotherapeutic agents that target fast dividing cells. Cytotoxic effects are also reduced by hypoxic stress proteins and decrease in apoptotic potential. Currently there is research being done into creating cytotoxic drugs selective for hypoxic cells.

Radiotherapy is also less effective in hypoxic tumours. The reason is because of the indirect damage caused by the free radical that is produced on absorption of radiation in tissue [11]. In comparison, in the absence of oxygen the amount of radicals that are formed by radiation is lower and therefore less damage is caused to DNA. Radiotherapy resistance could also possibly be caused by hypoxia-induced proteome and genome changes. These specific changes work by increasing the levels of heat shock proteins or otherwise reducing the apoptotic potential, both of which are linked to radio resistance.

Transient oxygenation of tumour tissues is also a barrier in cancer treatment. The reason for this is because transient hypoxia results in a decrease in cell viability whilst retaining full resistance to radiation. The reoxygenation of hypoxic cells also causes another problem, with each radiation fragment, cells are destroyed and neighbouring hypoxic cells reoxygenate.

The obvious reduction in radio sensitivity by hypoxia led to huge amounts of research into overcoming this problem. Some solutions for hypoxia modification are: high pressure oxygen chambers, hypoxic cell radiosensitisers, hypoxia mediated gene therapy and more [11] [12]. Although the modification of hypoxia results in some improved and better loco-regional control in tumours, huge improvements in a clinical outcome is difficult to prove. The main problem is that it is difficult to differentiate the specific tumours that would benefit from the modification of hypoxia [14].

Another effect of hypoxia is that it may encourage tumour progression regardless whether treatment has been administered or not. In this case it is hypothesised that the moderately hypoxic cells are the most important for studying the biological response of, as compared to highly hypoxic cells, which will ultimately die [25]. Therefore, recent efforts have been targeted towards anti-hypoxic treatments such as HIF-1 inhibitors, which aim to inhibit the tumour hypoxia response and raise the susceptibility of tumour cells to chemotherapy and radiotherapy.

Therefore, it is crucial to establish a reliable and reproducible measure of hypoxia so that it may greatly benefit patients that need to be identified in order to be given hypoxia modification therapies and anti-hypoxic treatments. Additionally, quantitative oxygen concentration (pO_2) maps could aid in adapting the radiation dose distributions in order to reduce the consequence of hypoxia. The integration of biological parameters in radiotherapy treatment is referred to as Biologically Guided Radiation Therapy (BGRT). Simulations of neck and head cancers have shown already that incorporating hypoxia information in radiation dose planning can hugely improve the tumour control probability [6]. BGRT has the potential to enhance local tumour control without greatly damaging normal tissue. However due to the complex cellular processes that are associated with hypoxia and reoxygenation of tumour tissue it may become necessary to repeat hypoxia measurements and recalculate the dose distributions during a radiotherapy treatment.

3.6 Oximetry

Hypoxia has a profound impact on tumour prognosis as well as treatment. Therefore constant research and investigation is directed towards measuring hypoxia [22]. Although there has been a significant amount of research that has been conducted in regards to measuring hypoxia, principal investigators in the field agree that until now there is no gold standard for measuring hypoxia. That is, the field of hypoxia measurements is still relatively new, the biology not completely understood yet and therefore it still unclear which is the ideal method to measure hypoxia. Also it is expected that no single method will be suitable for all cases and therefore the use of more than one method may be required. When assessing the potential of a new hypoxia measurement approach the following criteria should be taken into account:

- Invasiveness
- Robustness
- Accuracy
- Sensitivity: the dynamic range should allow the detection of pO_2 at levels that match to tumour therapy
- Spatial resolution or in global measurements the possibility to define the measurement value.

- Temporal resolution, etc. [7]

Additionally, hypoxia measurements techniques are categorised as direct or indirect methods. Indirect methods of measuring pO_2 observe metabolic reporters of oxygen levels, for example 2-nitroimidazole binding. Indirect methods give a signal in the absence of oxygen. Other methods are more focused on the biological response to hypoxia, for example, on the flow of blood, or deoxyhemoglobine-concentrations. Many of the current methods that are used to measure hypoxia lack spatial or temporal resolution, are highly invasive, non-quantitative or are not practical for longitudinal studies. For the purpose of this thesis we will study MRI as a means of measuring hypoxia. The next section elaborates on this method specifically.

3.6.1 Magnetic resonance imaging as a measuring technique

MRI is a powerful imaging technique and can be used for measurement in various approaches. Many of these approaches have target on imaging the oxygenation status of the tissue. In MRIs this is achieved by studying the paramagnetic effect of oxygen on NMR signals and relaxation times. However in order to correctly evaluate the paramagnetic effect of oxygen, relaxation times and quantitative measurements of NMR signals are required. It is essential to know the exact nature of the measured oxygenation quantity.

3.6.2 DCE MRI

In our study specifically we used the diffusion contrast enhanced (DCE) MRI in which the perfusion of injected contrast agent is analysed with kinetic models. By DCE-MRI measurements estimates can be derived of quantities such as vascular flow, perfusion and permeability. Based on those biological quantities, pO_2 can be derived using an extension of the Kroghs cylinder model.

Another approach using DCE-MRI for hypoxia measurements relies on the biochemical relations between hypoxia and permeability of blood vessels. Because of these relations DCE-MRI measured permeability can act as a surrogate marker for hypoxia. Although the reliability of this relation is questionable. Additionally, human application of DEC-MRI for tumour hypoxia study is unclear because of the unavailability of high molecular weight contrast agents that are more sensitive to permeability.

3.7 Conclusion

This chapter gives insight into a few concepts of oncology so as to appreciate the potential applications that quantitative MRI has to offer in the diagnosis and treatment of cancers. In summary, when cancer cells break out of the control mechanisms they uncontrollably divide and thus the cancer cell population grows progressively. The control mechanism is lost due to genetic mutations that deregulate the normal control mechanisms. The genetic

mutations are caused mainly carcinogenic agents such as chemicals and ionizing radiation. Cancer treatment requires a multidisciplinary approach which is achieved through chemo- and radiotherapy.

An advantage quantitative MRI is the imaging of hypoxia in cancerous tissue. Hypoxia, which is essentially low tissue oxygen concentration is a common characteristic feature of solid tumours. Its cause is mainly from inefficient tumour vascularisation. Hypoxia causes malignant tumour progression which leads to unfavourable disease prognosis. Moreover, the effects of hypoxia disrupt chemo- and radiotherapy. Therefore, the imaging of hypoxia could be integrated into radiotherapy treatment planning in order to improve the quality of the therapy. However, there is no gold standard till date on the way to measure hypoxia. A possible measurement method is ^{19}F MRI oximetry. This specific approach exploits the paramagnetic effect of oxygen on the T_1 relaxation time of fluorine containing compounds.

Chapter 4

Project model and methods

4.1 Introduction

In this chapter we will discuss the entire overview of the project. The project is simplified into two parts: the experimental procedure and the computational study. The two parts are further subdivided into tasks that were carried out and the methodology behind each of those tasks is elaborated in this chapter.

4.2 Project overview

The project's ultimate goal is to measure hypoxia in vivo. In order to achieve this there are many stages involved before obtaining the final result. For the purpose of this project we are studying how fast the concentration of the contrast agent, Gadolinium-DiethyleneTriaminePentacetate (Gd-DTPA) changes over time (further explained in Section 4.3 and 4.4). Fig. 4.1 consists of the flow chart of the whole project containing all the major steps carried out.

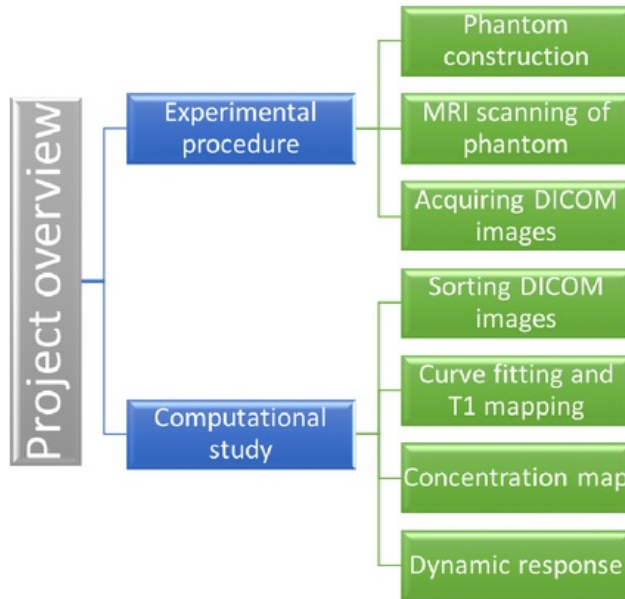


Figure 4.1: Flow chart of the project structure and the tasks involved

4.3 Experimental procedure

The objective of the study is to produce an experimental setup, i.e. construct a phantom (which is reproducible), for the purpose of simulating oxygen consumption by somatic cells in vivo and ultimately validating computational biophysical models of hypoxia with ^{19}F MRI oximetry. Initially we are measuring how fast the concentration of Gd-DTPA is changing over time in a region of interest so that we may eventually be able to deduce the cross-sectional diameter of the small capillaries in a voxel (all the MRI images of the experiment are made up of voxels, further explained in Section 4.3.2) and estimate the number of blood vessels in a voxel. Therefore, this experiment is one of the techniques involved that will aid in measuring the heterogeneity of a voxel. Then, with this knowledge it can be used as input for the computer simulations of oxygen concentration in a tumour.

The experimental setup is shown in Fig. 4.2. In our experimental setup we have a haemodialysis filter which models a tumour and it is made up of hollow, semi-permeable fibres which model tumour blood vessels. At a moment in time the contrast agent is injected into the system and it seeps into the tumour tissue, i.e. the outer compartment of the phantom. While the process is occurring the images are recorded on the MRI for a period of time. Eventually the bolus of contrast agent is washed out of the outer compartment of the phantom and it flows back into the reservoir of water as can be seen

in Fig. 4.2. As a result, it becomes a more diluted version of the contrast agent by mixing with the pool of water and then is pumped back into the phantom.

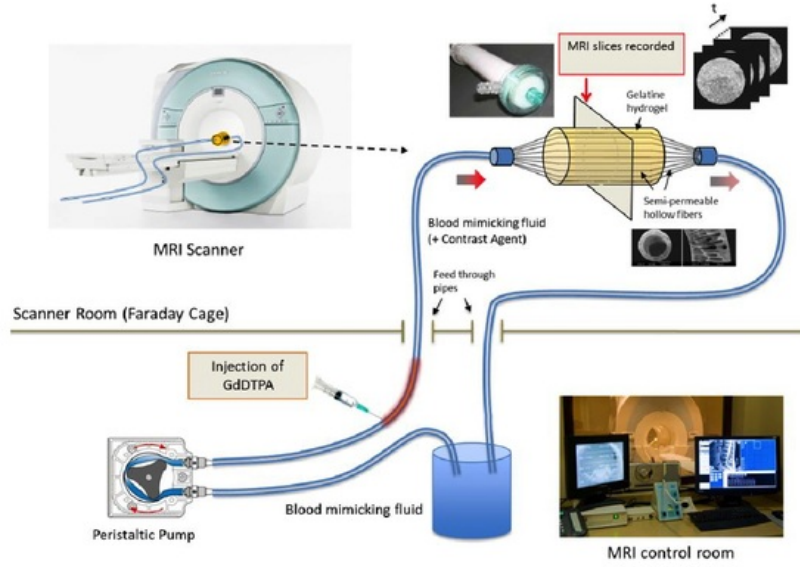


Figure 4.2: The experimental setup for MRI scanning [9]

4.3.1 Phantom construction

The main component of our experimental model is the phantom which comprises of a haemodialysis filter. The haemodialysis filter is filled with hollow fibres which run across the axis of the cylinder. In our experimental model, these hollow fibres mimic human blood vessels. The blood-substituting fluid was pumped through the inner compartment of the filter, i.e. through the lumen of the fibres. The outer compartment of the haemodialysis filter was used for the dialysate fluid which simulates tissue and was filled with a gelatin matrix. For the purpose of our study, i.e. studying the perfusion of the contrast agent, the matrix is simply filled with a solution of 6%(w/w) concentration of gelatin mixed with water, 0.2%(w/w) sodium azide (an antifungal agent) and the rest is water. The structure of the phantom can be seen in Fig.4.3.

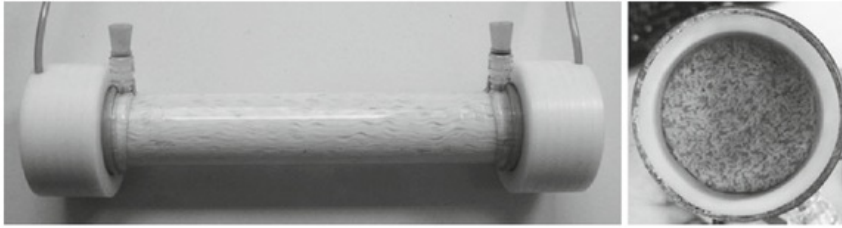


Figure 4.3: (left) Side view of the phantom with connections to the inner compartment at the sides of the filter and connections to the outer compartment filled with hydrogel. (right) Opened entrance part of the inner compartments of the haemodialysis filter showing the hollow fibres. [19]

In the future, when we would use ^{19}F MRI oximetry to model hypoxia, this gelatin matrix would be filled with yeast cells which is representative of oxygen-consuming tissue. Moreover, in conditions of oxygen deprivation the yeast cells switch to anaerobic respiration which makes the phantom usage ideal as it does not have to be continuously respired. The haemodialysis filter itself was preheated in a water bath at approximately 35°C to allow the hydrogel to circulate with ease. Hydrogel is pumped in a closed circuit in an attempt to minimise the air bubbles emerging from the filter. The inner compartment of the filter was filled with N_2 and the phantom was then left for 2-4 hours. Lastly when the gel had solidified the inner compartment was prefilled with (de-oxygenated) water (or otherwise the blood-substituting fluid) to begin the scanning. In our experimental model the flow of blood in the phantom is simulated by a peristaltic pump. The speed of the pumping of the blood-simulating fluid was 60 rpm and the flow rate was 590 ml/min.

4.3.2 MRI scanning of the phantom

The scanning was conducted by the SIEMENS Magnetom Verio clinical MRI scanner at Macquarie University Hospital. For our study, we used the Dynamic Contrast Enhanced (DCE) MRI imaging sequence and observed the inversion recovery sequence. Once, we had begun the scanning at a magnetic field of 3T, at a certain point in time the contrast agent, Gd-DTPA was injected and the images were recorded over time.

A total of 771 images were recorded from the scan. Each image is a T_1 weighted image that is made up of voxels. Voxels are similar to pixels except that they have a certain thickness. Each image is a matrix of size 128 voxels x 128 voxels.

4.3.3 Acquiring DICOM images

In this study, all the images acquired were T_1 weighted images. T_1 weighted images are used to mainly differentiate anatomical structures on the basis of their T_1 values. It is essentially a pulse sequence and relies on the longitudinal relaxation of a tissues net magnetisation vector. The protons spins that are aligned in the direction of the external

magnetic field (B_0) are transferred into the transverse plane by an RF pulse and eventually slide back towards the initial equilibrium of B_0 . However, not all tissues are able to get back to the original equilibrium position quickly and hence, a tissues T_1 value is reflective of the amount of time it takes for the protons spins to realign themselves into the direction of the main magnetic field (B_0) [2].

The MRI scanning conducted was using the DCE-MRI (Dynamic Contrast Enhanced-Magnetic Resonance imaging) sequence. DCE-MRI reveals the changes in the microvasculature of tumours as quite often tumours contain leaky blood vessels. T_1 weighted DCE-MRI images were attained of the phantom at different inversion times (TI) starting from 30 milliseconds to 450 milliseconds in intervals of 20 milliseconds, this was done in order to observe the change in signal intensity within all the voxels of an image. Additionally, the DCE-MRI was also used to acquire images after Gd-DTPA was injected into the phantom and from those images quantitative parametric maps were created (see Chapter 5). The following Fig.4.4 shows the file contents of an image.

Original File - Outside Phantom						Modified File - Outside Phantom					
	1	2	3	4	5		1	2	3	4	5
1	2048	2048	2048	2048	2048	1	0	0	0	0	0
2	2048	2057	2051	2054	2041	2	0	9	3	6	-7
3	2048	2048	2043	2041	2049	3	0	0	-5	-7	1
4	2048	2060	2044	2043	2062	4	0	12	-4	-5	14
5	2048	2047	2056	2040	2039	5	0	-1	8	-8	-9
6	2048	2045	2046	2054	2053	6	0	-3	-2	6	5
7	2048	2048	2038	2055	2064	7	0	0	-10	8	16
8	2048	2061	2045	2049	2059	8	0	13	-3	1	11
9	2048	2037	2059	2050	2058	9	0	-11	11	2	10
10	2048	2042	2043	2061	2038	10	0	-6	-5	13	-10
11	2048	2045	2039	2049	2060	11	0	-3	-9	1	12
12	2048	2045	2050	2057	2059	12	0	-3	2	9	11

Original File - Inside Phantom						Modified File - Inside Phantom					
	58	59	60	61	62		58	59	60	61	62
75	2859	2876	2814	2795	2853	75	811	828	766	747	805
76	2819	2864	2871	2881	2829	76	771	816	823	833	781
77	2762	2835	2889	2932	2868	77	714	787	841	884	820
78	2834	2864	2935	2915	2854	78	786	816	887	868	806
79	2886	2878	2917	2892	2827	79	840	830	869	844	779
80	2814	2826	2822	2840	2835	80	766	778	774	792	787
81	2817	2864	2886	2910	2868	81	769	816	838	862	820
82	2870	2858	2874	2919	2858	82	822	810	826	871	810
83	2831	2823	2830	2888	2899	83	783	775	782	840	851
84	2802	2782	2833	2841	2863	84	754	734	785	793	815
85	2892	2856	2919	2838	2842	85	844	808	871	790	794
86	2783	2866	2919	2846	2866	86	735	818	871	798	818

Figure 4.4: The signal intensity (S_i) values outside and inside the phantom. The values in the original file have an offset of 2048, the modified file subtracts the offset to obtain the actual contrast.

It consists of a matrix (of size 128 voxels by 128 voxels) that is representative of the signal intensity (S_i) value of each voxel. The Fig. 4.4 shows an original file and modified file this

is because in order to have the correct contrast values 2048 needs to be subtracted from all the values. The offset of 2048 comes from the fact that SIEMENS MRI scanners scales the phase from $(-\pi, \pi)$ to $(0, 4096)$ with 2048 being zero phase. All white matter in an image has a phase of 0 Radians, which is 2048 in SIEMENS phase units [10].

4.4 Computational study

For the first part of the computational study, we observed the change in signal intensity within all image voxels of the T_1 weighted images at the specific inversion times. We used the inversion recovery sequence because it provides image contrasts in which it is possible to selectively suppress or null the signal from a given tissue based on its T_1 value, it has twice the sensitivities to T_1 differences as compared to other sequences which means that it will give a high T_1 -weighted contrast and lastly, it is additive rather than competitive T_1 and T_2 contrast. More information about the inversion recovery sequence can be read in Chapter 2.

Then, from the plot of signal intensity over inversion time unique T_1 values and S_0 values were extracted by applying a curve fit. The T_1 and S_0 values were transferred into individual matrices and hence, the T_1 map was plotted as shown in Fig. 5.2. Finally, the concentration map was derived to illustrate how fast the concentration of Gd-DTPA changes over time (explained in detail in Section 4.4.3).

4.4.1 Sorting DICOM images

All T_1 weighted images obtained were with the use of the 3T clinical MRI scanner. The standard constant imaging parameters for the images were as shown in the following Tab. 4.1.

Size of image	128×128
Repetition time	1000 ms
Echo time	13 ms
Slice thickness	5 ms
Flip angle	180°
Echo train length	15

Table 4.1: Standard imaging parameters during MRI scanning

As we were studying the inversion recovery sequence, all the images had varying inversion times. In order to map the signal intensity of each voxel over the inversion time (TI) using Eq. 4.1, the first step was to sort the T_1 weighted data (i.e. 771 image files) to extract the relevant images. For the purpose of our study, we were interested in the images that had $TI = [30ms \ 450ms]$ in intervals of 20ms and $TI = 100ms$. We filtered the relevant image

files by writing a program in MATLAB which is given in Appendix B. This program does the following things,

- Reading all the IMA files (771 images) that were scanned during the experiment.
- Extracting the required parameters (i.e. Patient name, Series number, Instance number, Acquisition time) and combining them to output as the new name of the file.
- Copying the files and saving them into a new directory with new name.

There were two sets of 22 files with the $TI = [30\ 450]$ with an interval of 20ms. One set represents images before the contrast agent and other after the contrast agent. There were 186 files with $TI = 100ms$. 12 of these files were taken before contrast agent and rest were taken after. Thus, all these files were extracted and used for further study.

4.4.2 Curve fitting and T_1 mapping

The next task was to create a graph of signal intensity over the inversion time. The Signal intensity (S_i) equation for the inversion recovery sequence is:

$$S_i = S_0(1 - 2e^{-\frac{TI}{T_1}}) \quad (4.1)$$

Where, S_0 is the observed signal intensity when there are no magnetisation pre-pulses applied or when there is no contrast agent and TI is the inversion time which is divided by the T_1 value. In the equation, S_0 and T_1 are unknowns and essentially that is what we will be deriving from the plots.

As discussed earlier, there were 22 files (each file 128×128) with varying $TI = [30ms\ 450ms]$ with 20ms intervals. These files were used to find the unknowns S_0 and T_1 of the Eq. 4.1. A curve fitting algorithm was applied to each corresponding entry of the 22 files. And hence, by applying curve fitting algorithm 16,384 times (i.e. all entry), we extracted two 128×128 matrices for the unknowns S_0 and T_1 . The MATLAB code for the curve fitting algorithm can be seen in Fig. 4.5.

```

72 % Step 3: Curve Fitting
73 - functn = @(c,ti) c(1)*(1-2*exp(-ti/c(2))); %input function
74
75 - T_1 = zeros(128, 128); %Matrix to store T1 values
76 - S_0 = zeros(128, 128); %Matrix to store S0 values
77 - x = 1; y = 1; % x and y-coord of t1 matrix
78 - count = 128*128;
79 - for i = 1:(128*128)
80 -     B = A(i,:);
81 -     c0 = [500, 2]; %initial guesses for parameters
82 -     psolve = lsqcurvefit(functn, c0, ti, B); %Curve Fitting
83 -     S0 = psolve(1); t1 = psolve(2); % solved parameters
84 -     S_0(x,y) = S0; T_1(x,y) = t1; %Storing the unknowns in the Matrix
85 -     y = y + 1; %Updating the column
86 -     if (y ==129) % resetting the column to change to new row
87 -         y = 1;
88 -         x = x+1;
89 -     end
90 -     count = count -1
91 - end

```

Figure 4.5: MATLAB Code for Curve fitting using Eq. 4.1

Hence, the T_1 matrix was converted to greyscale image and then stored as a DICOM image file (i.e. known as T_1 map). The complete MATLAB code can be seen in Appendix C). This code executes the following tasks:

- Reading 22 files and storing the data all of them in one matrix ($16,384 \times 22$), i.e. each column represents one file.
- Plotting a few graphs of the signal intensity vs TI both, outside and inside the phantom.
- Fitting Curve to the Eq. 4.1 to find the unknowns S_0 and T_1 .
- Converting the T_1 matrix to greyscale and storing it as a DICOM image.
- Plotting a few sample of curve fitting and raw data to compare the accuracy of curve fitting.

4.4.3 Concentration map

The concentration map was evaluated using the parameters of T_1 and S_0 from Section 4.4.2 and the files with TI = 100ms. As discussed earlier, 186 images were taken at TI = 100ms. 12 of these images were taken before contrast agent. Immediately after the 12th image, the contrast agent was injected into the system. Thereafter in intervals of 10 seconds, 186 images were recorded of the phantom in order to study the perfusion of Gd-DTPA into the phantom system. The contrast agent concentration is then derived

from the change in relaxation rate using a linear relationship.

$$R_1 = R_1^0 + rC \quad (4.2)$$

$$C = \frac{R_1 - R_1^0}{r} \quad (4.3)$$

Where, C is the concentration in a voxel, R_1 is the relaxation rate after the contrast agent was injected, R_1^0 denotes the relaxation rate before the contrast agent was injected and r is the relaxivity of the contrast agent, i.e. Gd-DTPA which is 3 m/L. R_1 and R_1^0 are the unknowns and it is discussed below how they are evaluated.

First we calculated R_1 . The relationship between R_1 and T_1 is given in the following equation:

$$R_1 = \frac{1}{T_1} \quad (4.4)$$

The equation for R_1 is derived from Eq. 4.1 and 4.4, and it is given below:

$$R_1 = \frac{1}{TI} \ln\left(\frac{S_i - S_0}{2S_0}\right) \quad (4.5)$$

Hence by solving the Eq. 4.5, R_1 was determined, where $TI = 100\text{ms}$, S_0 matrix is same as Section 4.4.2 and S_i the signal intensity of files after contrast agent injected at $TI = 100\text{ms}$.

Then, R_1^0 was evaluated from the Eq. 4.4 using the T_1 matrix determined in Section 4.4.2. Hence, after determining R_1 and R_1^0 the Concentration (C) was evaluated using Eq. 4.3. The MATLAB code for this section can be viewed in the Appendix D. This code executes the following tasks:

- Finding R_1^0 matrix from the T_1 matrix (Note: T_1 see Section 4.4.2)
- Solving the Eq. 4.5 to determine R_1 matrix for each image file.
- Finding Concentration (C) matrix for each file using Eq. 4.3.
- Picking a few patches in side the phantom and averaging their concentration values for Dynamic response (will be discussed in Section 4.4.4).
- Plotting some samples of Dynamic response and Concentration map (both on the same graph).

4.4.4 Dynamic response

Dynamic response was observed by taking a region of interest inside the phantom at various points, as can be seen in the following schematic representation of the image of the phantom and the highlighted regions of interest. It was achieved by defining a patch or smaller matrix around the point of interest and taking the average of all the concentration values in that patch. These smaller patches inside the phantom are illustrated in Fig. 4.6.

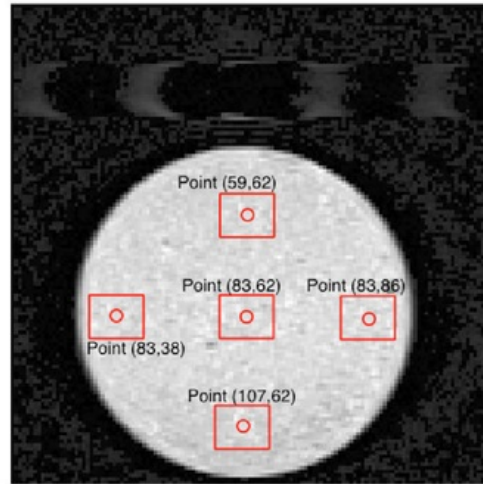


Figure 4.6: A schematic representation of the points from which the concentration maps were derived. The borders around each point indicate the regions which were used for each respective point to calculate the dynamic response.

The purpose of the dynamic response is to study the fluctuations in concentration of the contrast agent specifically inside the phantom. A more detailed explanation is provided in Chapter 5.

Chapter 5

Results and Discussion

5.1 Introduction

This chapter presents and discusses the results obtained of each step that was carried out in the computational study (Section 4.4) of the project.

5.2 Curve fitting and T_1 map

The inversion recovery sequence begins with a 180 inversion of the RF pulse. As a result, the pulse flips the longitudinal magnetisation vector from the x-y plane into the z direction. Eventually, the longitudinal magnetisation grows back after the external inversion pulse is switched off. This is known as the T_1 recovery. The reconstruction process of the inversion recovery images is sensitive only to the magnitude of the magnetisation of a tissue regardless of whether it is positive or negative [17]. This can be seen in Fig. 5.1 below, where the positive or negative values are dependent on the inversion times. Smaller inversion times, such as from 30ms- 70ms have negative signal intensities, whereas higher inversion times such as greater than 110ms have positive signal intensity values.

As discussed earlier, the purpose of the curve fitting on the signal intensity over inversion time plots was to extract the T_1 and S_0 values. T_1 relaxation time tells how fast proton recovers in the z-axis after being flipped by RF Pulse. T_1 Map is an MRI image, in which each pixel corresponds to a T_1 relaxation time. In a T_1 Map, the brighter areas correspond to tissue with a fast T_1 value that has recovered the most signal in the repetition time. Whereas, darker areas are associated with tissues with slow T_1 value, i.e. high water content regions. After all the T_1 values were found, the T_1 map was made which is shown in Fig. 5.2.

However, initially T_1 map was almost white coloured. It was investigated that some of the T_1 values (outside the phantom i.e., outside the area of interest) were too large or too small. It can be seen that in Fig. 5.1 (a), at the point (15,80) which is outside the phantom, when the curve fitting was applied it intersected the least amount of points and

the majority of the points were scattered randomly. Because of that, the curve fitting wasn't effective and there were a few huge T_1 values were calculated. Some of these random values were in the order of -10^8 or $+10^8$. Since, T_1 map is based on relative values of whole matrix scaled between 0 to 65,535, that's why the image wasn't clear. Note that these abnormal values were only found outside the phantom. Therefore, all those random values were replaced with the average values of the surrounding points in order to obtain a more precise T_1 map.

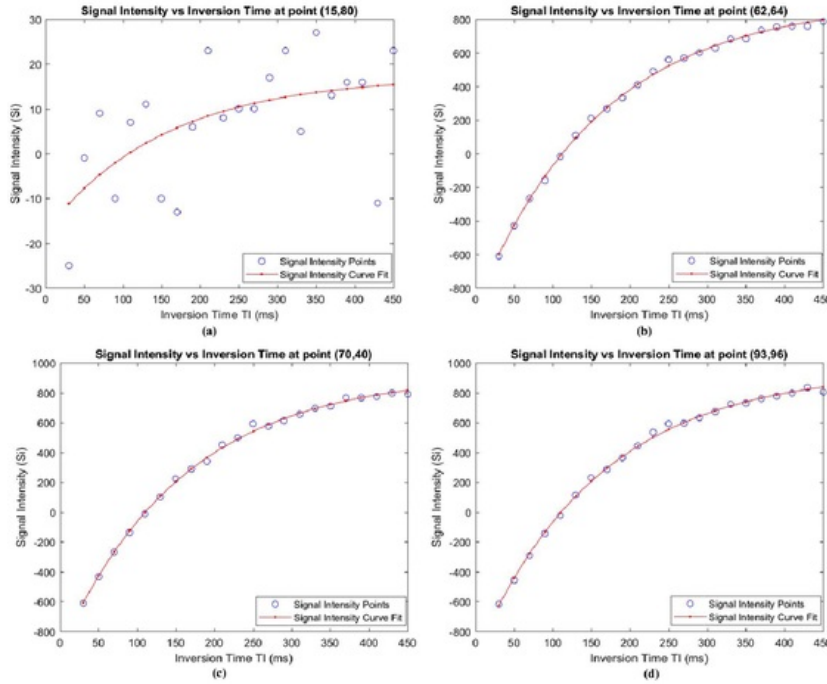


Figure 5.1: (a) Represents point outside the phantom (b)-(d) Represents points inside the phantom.

It can be seen that the value of T_1 map in Fig. 5.2 (a), before the contrast agent was injected, is greater than the value of T_1 map in Fig. 5.2 (b), after the contrast agent was injected. This is because Gd-DTPA has the effect of shortening T_1 relaxation times and hence, increasing the signal intensity which was expected theoretically.

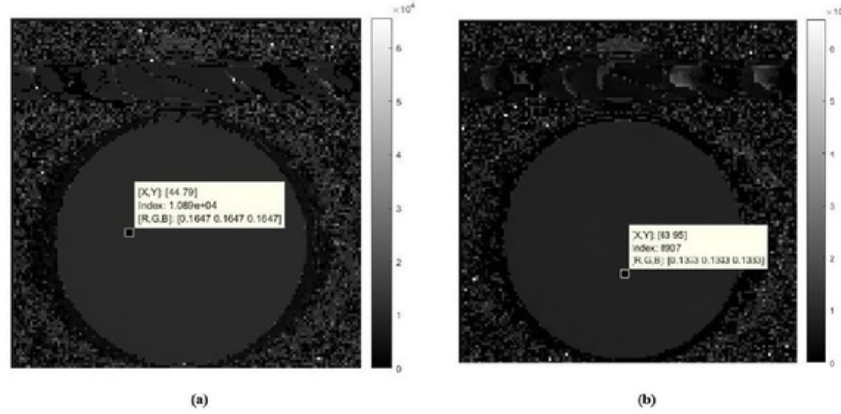


Figure 5.2: (a) T_1 map before contrast agent was injected. (b) T_1 map after contrast agent. The contrast agent shortens T_1 values.

5.3 Concentration map

Low- molecular weight extracellular contrast agents, such as Gd-DTPA diffuse readily into the extracellular extravascular space of a blood vessel. This is represented in our phantom model whereby, the haemodialysis fibres mimic the blood vessels and the outer compartment resembles tissue. In contrast agents, the contrast is caused mainly by its paramagnetic center and the rotational correlation time. T_1 and T_2 are both affected by paramagnetic contrast agents. In T_1 weighted imaging sequences, the presence of these contrast agents causes signal enhancement in the images.

In our experiment at the inversion time of 100ms, 12 images were recorded in intervals of 10 seconds and immediately, after the 12th image, a bolus of Gd-DTPA was injected into the system. In in vivo studies, this would mean that bolus of contrast agent would be injected intravenously into a patient. The contrast agent that is now carried in the blood, travels into the blood vessel of a tumour. While the contrast agent is in the blood vessel of the tumour it leaks into the tumour tissue, or Extracellular Extravascular Space (EES) and remains there for a while. The leakage is a result of damaged blood vessels in the tumour. After a moment in time fresh blood travels into the blood vessel of the tumour with no contrast agent as it now washed out, but the leakage of the contrast agent remains in the tissue for a while. What results is a diffusion gradient between the blood vessel and tissue. Well vascularised tissue show fast signal increase, whereas poorly vascularised tissue (for e.g. necrotic tissue) will show a slower signal enhancement. Eventually, the contrast agent leaks back into the blood vessel and it slowly disappears and moves out of tissue. Contrast agent moves out even slower from necrotic tissue.

After the uptake phase of the contrast agent an equilibrium phase is established. The

equilibrium is established between the constant flow and inflow of the contrast agent. This is a result of the contrast agent being equally distributed between blood vessels and EES of tissue and therefore there is no change in signal intensity. Eventually over a period of time, the contrast agent becomes more diluted than its initial concentration and begins to get cleared out by a diffusion driven washout from the EES.

In Fig. 5.3, three distinct phases can be recognized as was previously discussed. The interpretation of these graphs is as follows: Initially, there is an uptake phase at the time of 120 seconds, i.e. as soon as the contrast agent was injected. This means that there is a high concentration of contrast agent in the haemodialysis fibres (blood vessel) than in the outer compartment (tissue). Eventually, as the contrast agent infiltrates from the blood vessel into the tissue it slowly becomes equally distributed over both compartments. Finally, the concentration of the contrast agent begins to decrease as each time it gets pumped out of the system it becomes diluted by mixing in the reservoir of water. As the contrast agent is pumped back in to the phantom it decreases in concentration, eventually reaching an equilibrium. This was expected as the experimental model is a closed system and hence, the concentration would become stable.

5.4 Dynamic Response

The concentration map illustrates the perfusion of Gd-DTPA at a point in the experimental model over a period of time, whereas, the dynamic response illustrates the perfusion of the contrast agent in a region in the experimental model. The comparison of the concentration map and dynamic response at different regions is given in Fig. 5.4. The dynamic response is basically derived from taking the average of smaller matrices of the concentration inside the phantom region. These regions have been shown in Fig. 4.6.

By comparing the concentration map (orange line in Fig. 5.4) with dynamic response (blue line in Fig. 5.4), the pattern of both the curve are similar to each other, where the concentration map is just at one point (may resemble one cell) and the dynamic response is more specific to what is occurring directly in the tumour tissue. Therefore, the dynamic response can be used similarly in a way to determine the amount of oxygen that diffuses into tumour tissue in future works using ^{19}F MRI oximetry techniques.

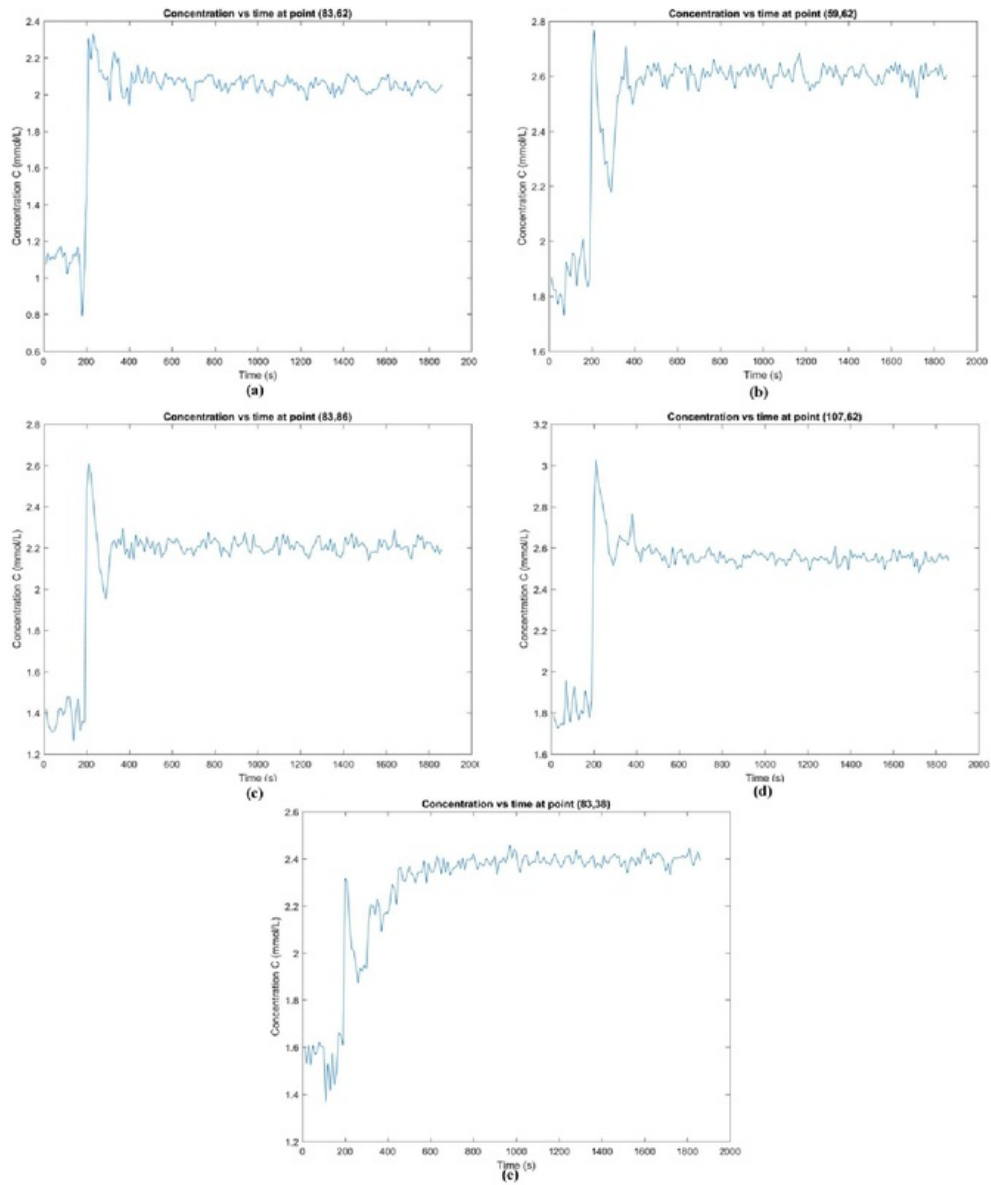


Figure 5.3: Change in concentration of Gd-DTPA over time at various points inside the phantom

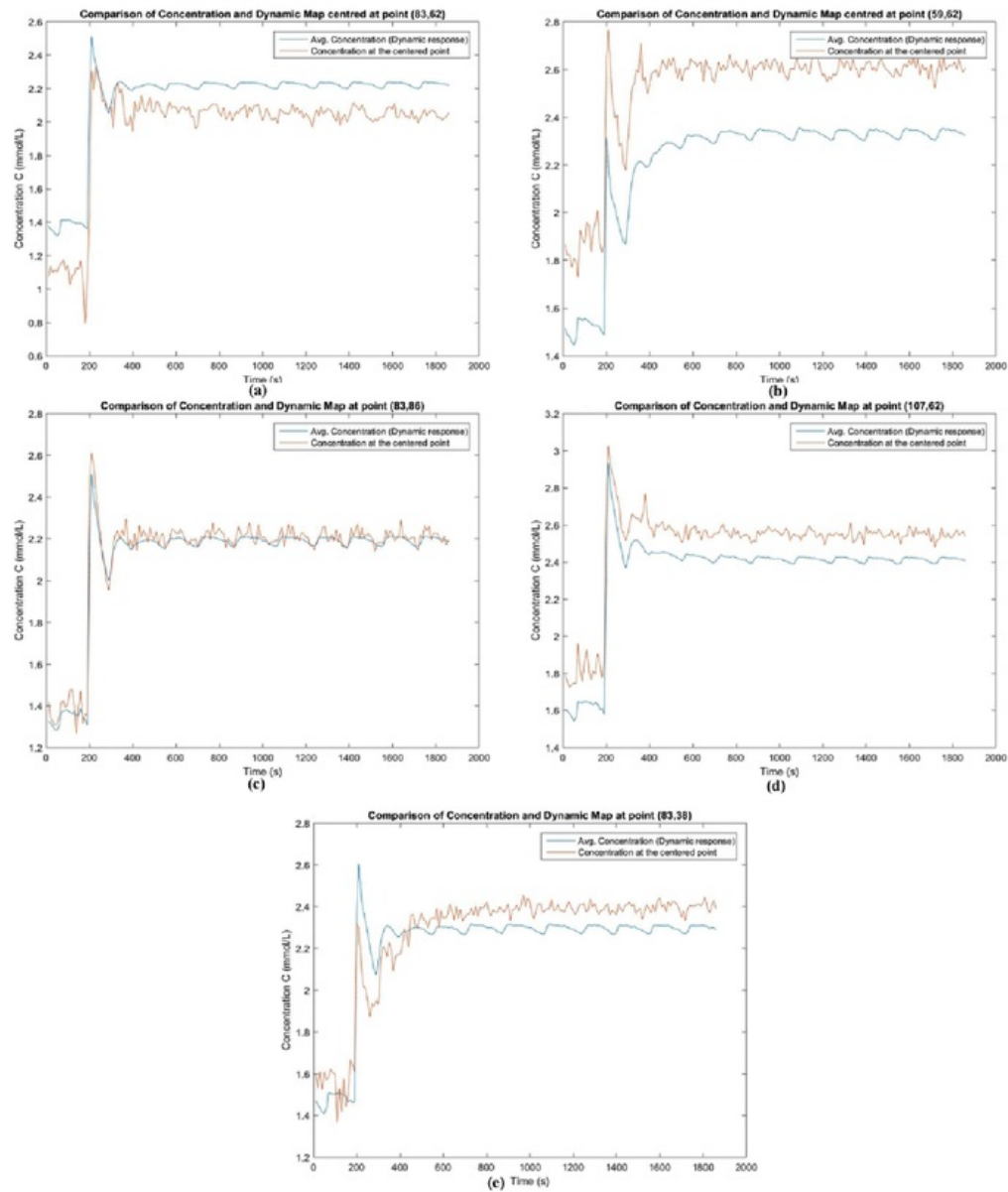


Figure 5.4: Dynamic response at various points inside the phantom as marked in Fig. 4.6

5.5 Conclusion

One of the most common causes of tumour hypoxia is diffusion related hypoxia which is caused by increased oxygen diffusion distances. Tumour cells are forced to move away from perivascular areas by the pressure of proliferation as a result the cells that are located past the oxygen diffusion boundary suffer from insufficient oxygen supply. The bigger purpose of this study is to quantify the amount of oxygen that diffuses past the diffusion gradient between tumour tissues and blood vessels. The contrast agent experiment models this whereby Gd-DTPA leaks into the outer compartment of the phantom (mimicking tumour tissue). In the above dynamic response (Fig. 5.4) we can observe the changes in the concentration of the contrast agent over time. Although this is not a map of oxygen concentration it is the initial step in deriving the oxygen map. The oxygen concentration map can be derived from ^{19}F MRI oximetry, which is further elaborated in Chapter 6.

Chapter 6

Conclusion and future works

6.1 Conclusion

Images that are acquired from the DCE MRI scan are entirely composed of pixels, or specifically known as voxels. Voxels are essentially three dimensional pixels. In each voxel there are cells that have high concentration of oxygen and some cells which have low concentration of oxygen what we see is simply the average value of the oxygen distribution in that pixel. The problem lies in the fact that this average value is not an accurate representation of distribution of the concentration of oxygen, we want to know the exact number of cells which have a certain level of oxygen concentration below a certain threshold. This kind of problem is called intravoxel heterogeneity, i.e. the oxygen concentration is heterogeneous in a voxel and we need to establish a method to measure this heterogeneity.

Ultimately, the purpose of this study on a broader perspective is to carry out this measuring procedure in vivo to map oxygen concentration and produce simulations of how oxygen perfuses in tumours of cancer patients in order to deliver more effective radiotherapy. Therefore, to map the concentration of oxygen it is essential to know how many blood vessels are in each voxel as well as the size of the blood vessels, then it can be used as an input for computing simulations. Together with the simulations of how oxygen perfuses within tumour tissue and this average value represented by a voxel we can model this and then we can derive how heterogeneous a voxel is, this cannot be achieved by just looking at the voxel because the voxel could be completely heterogeneous or completely homogenous, or in between. In order to measure this, this is where our experiment with the contrast agent comes in. The purpose of this experiment was to measure the perfusion of the tumour with blood by injecting a contrast agent and measuring how fast the concentration changes within a voxel.

This experiment is one technique amongst the numerous techniques that are involved in determining the heterogeneity of voxel (other values such as $R2^*$ also need to be calculated). This measure is then incorporated into the 19-Fluorine T_1 measurements for oxygen concentration determination. We started with the contrast agent experiment to

understand the dynamics with the contrast agent because the next step involves using a completely new nucleus, i.e. 19-Fluorine and that is a challenging task on its own.

6.2 Future works

The overall objective of this study was to improve cancer therapy prognosis by incorporating information about the oxygenation status of tumours in the novel cancer treatment methods. A huge amount of effort has been put into deriving methods to measure oxygenation status of tumours, however no gold standard method has been declared till date.

A non-invasive MRI technique to measure the oxygenation status of tumour tissue is by ^{19}F MRI. ^{19}F MRI oximetry makes it possible to make sensitive and quantitative measurements of interstitial oxygen concentrations. ^{19}F is an abundant natural and stable isotope of Fluorine however it does not occur in sufficient concentrations in vivo in order to be detected with MRI. Instead, in ^{19}F MRI oximetry a Fluorine-containing compound (perfluorocarbon, PFC) is used as an oxygenation marker in tumour tissue. It is known that the longitudinal relaxation rate (R_1) of PFCs increases linearly with the dissolved oxygen concentration ($p\text{O}_2$) because of the paramagnetic effect of oxygen molecules. This property of PFCs makes it an ideal probe for measuring oxygen concentrations non-invasively. And thus this linearity can be exploited for in vivo imaging of oxygen concentration in tumour tissue.

In our experimental setup we would modify the phantom by filling the outer compartment with a gelatin matrix consisting of viable yeast cells. Tumour tissue is modelled by the outer compartment of the phantom which is comprised the yeast cells. Yeast cells consume oxygen when oxygen is made available, similar to real tissue. The blood simulating fluid that in this experiment would be composed of hexafluorobenzene, which is a PFC.

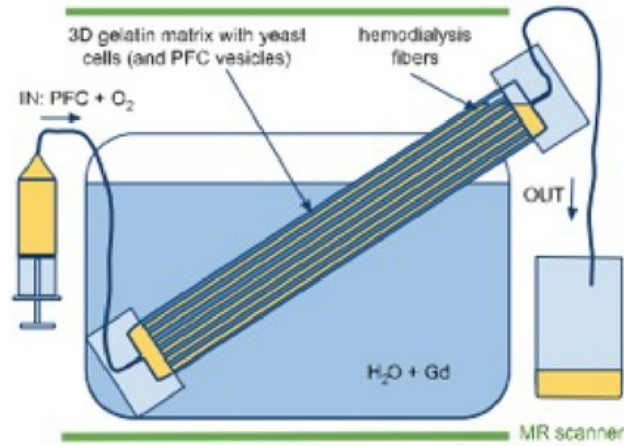


Figure 6.1: A schematic representation of the experimental setup of a phantom for the quantitative ^{19}F MRI-oximetry method [19]

The hexafluorobenzene supplies oxygen to the yeast cells in the phantom as it has a good oxygen solubility. The PFC also serves as a marker of the oxygenation status of the tissue. The R_1 relaxation rate in the phantom would then be measured in certain time intervals with the qTOMROP sequence. The resulting R_1 would then be used to derive the $p\text{O}_2$ maps using the calibrated R_1 ($p\text{O}_2$) relation. In conclusion the experiment incorporating ^{19}F oximetry can be used to simulate the consumption of oxygen by somatic cells in vivo, for modelling different hypoxia situations and for the comparison of ^{19}F oximetry markers and different methods.

Bibliography

- [1] "mri hardware." [Online]. Available: <http://www.starfighter.acornarcade.com/mysite/articles/Images/aiesay/Pic3.png>
- [2] "T1 weighted image." [Online]. Available: <https://radiopaedia.org/articles/t1-weighted-image>
- [3] "World health organisation: Cancer fact sheet." [Online]. Available: <http://www.who.int/mediacentre/factsheets/fs297/en/>
- [4] "Mri's inside story," 2003. [Online]. Available: <http://www.economist.com/node/2246166>
- [5] "A quick history of the mri," 2009. [Online]. Available: <http://www.two-views.com/mri-imaging/history.html#sthash.17I2j8QV.dpbs>
- [6] O. B. S. B. A. Sovik, E. Malinen and D. Olsen, "Optimisation of tumour control probability in hypoxic tumours by radiation dose redistribution: a modelling study." *Phys. Med. Biol.*, 2007.
- [7] S. Baete, "Quantitative nuclear magnetic resonance imaging for characterisation of biologically relevant parameters for cancer therapy," Ph.D. dissertation, Ghent University, February 2011.
- [8] S. R. Brown, M., *MRI basic principles and applications*. Wiley-Liss.
- [9] Y. Deene, "Quantitative mri," *Macquarie University, Sydney*, 2014. [Online]. Available: <http://science.mq.edu.au/~dyves/research/qmri.html>
- [10] Z. W. M. Haacke, "Identification of calcification with magnetic resonance imaging using susceptibility-weighted imaging: A case study," *J Magn Reson Imaging*, 2009.
- [11] E. Hall, *Radiobiology for the Radiologist*. Lippincott Williams and Wilkins, 2006.
- [12] A. B. H.L. Janssen, K.M Haustermans and A. Begg., "Hypoxia in head and neck cancer: how much, how important," *Head neck*, 2005.
- [13] M. Hockel and P. Vaupel, "Tumour hypoxia: definitions and current clinical, biological and molecular aspects," *J. Natl. Cancer Inst.*, 2001.

- [14] J. L. K.A. Krohn and R. Mason, "Molecular imaging of hypoxia," . *J. Nucl. Med.*, 2008.
- [15] V. Kuperman, *Magnetic resonance imaging physical principles and applications*. Academic Press.
- [16] S. R. McKeown, "Defining normoxia, physoxia and hypoxia in tumoursimplications for treatment response," *Br. J. Radiol.*, 2014.
- [17] M. Nazarpour, "The effect of inversion times on the minimum signal intensity of the contrast agent concentration using inversion recovery t1-weighted fast imaging sequence," *Med J Islam Repub Iran.*, 2014.
- [18] E. Podgorsak, *Radiation oncology physics: A handbook for teachers and students*. International Atomic Energy Agency, 2005.
- [19] L. C. W. N. Y. S. Baete, J. Vandecasteele, "An oxygen-consuming phantom simulating perfused tissue to explore oxygen dynamics and 19f mri oximetry," *Magn Reson Mater Phy*, 2010.
- [20] E. Y. K. S. T. M. Sara Rockwell, Iwona T Dobrucki and V. T. Vu, "Hypoxia and radiation therapy: Past history, ongoing research, and future promise," *Curr. Mol. Med*, 2009.
- [21] S. S. Takashi Hashido, "Quantitative t1, t2, and t2* mapping and semi-quantitative neuromelanin-sensitive magnetic resonance imaging of the human midbrain," *PLOS*, 2016.
- [22] J. TatumD.Sullivan, "Hypoxia : Importance in tumour biology, non-invasive measurement by imaging, and value of its measurement in the management of cancer therapy," *Int. J. Radiat. Biol.*, 2006.
- [23] P. Vaupel, "The role of hypoxia-induced factors in tumor progression," *The Oncologist*, 2004.
- [24] W.Denny, "The role of hypoxia-activated prodrugs in cancer therapy," *The Lancet Oncology*, 2000.
- [25] B. Wouters and J. Brown, "Cells at intermediate oxygen levels can be more important than the hypoxic fraction in determining tumour response to fractionated radiotherapy." *Rad. Res.*, 1997.

Appendix A

More about hypoxia

Received:
22 October 2013

Revised:
23 December 2013

Accepted:
2 January 2014

doi: 10.1259/bjr.20130676

Cite this article as:

McKeown SR. Defining normoxia, physoxia and hypoxia in tumours—implications for treatment response. Br J Radiol 2014;87:20130676.

RADIOBIOLOGY SPECIAL FEATURE: REVIEW ARTICLE

Defining normoxia, physoxia and hypoxia in tumours—implications for treatment response

S R MCKEOWN, MA, PhD

Biomedical Sciences Research Institute, University of Ulster, Coleraine, Northern Ireland, UK

Address correspondence to: Professor Stephanie Ruth McKeown

E-mail: sr.mckeown@ulster.ac.uk

ABSTRACT

Tumour hypoxia is increasingly recognized as a major deleterious factor in cancer therapies, as it compromises treatment and drives malignant progression. This review seeks to clarify the oxygen levels that are pertinent to this issue. It is argued that normoxia (20% oxygen) is an extremely poor comparator for “physoxia”, i.e. the much lower levels of oxygen universally found in normal tissues, which averages about 5% oxygen, and ranges from about 3% to 7.4%. Importantly, it should be recognized that the median oxygenation in untreated tumours is significantly much lower, falling between approximately 0.3% and 4.2% oxygen, with most tumours exhibiting median oxygen levels <2%. This is partially dependent on the tissue of origin, and it is notable that many prostate and pancreatic tumours are profoundly hypoxic. In addition, therapy can induce even further, often unrecognized, changes in tumour oxygenation that may vary longitudinally, increasing or decreasing during treatment in ways that are not always predictable. Studies that fail to take cognizance of the actual physiological levels of oxygen in tissues (approximately 5%) and tumours (approximately 1%) may fail to identify the real circumstances driving tumour response to treatment and/or malignant progression. This can be of particular importance in genetic studies *in vitro* when comparison to human tumours is required.

In the 1950s, tumour hypoxia was barely acknowledged, as evidenced by the paucity of publications on this subject; this is in contrast to the 10 000 articles that have been published over the last decade (Figure 1). However, since the seminal publications of Gray et al,^{1,2} the radiobiology and radiotherapy (RT) communities have acknowledged the importance that oxygen plays to RT responses. There is abundant and convincing evidence that RT is more effective against better-oxygenated cells, whereas hypoxic cells are significantly more radioresistant, with a marked fall in sensitivity below 2.6% oxygen (20 mmHg), which is particularly precipitate below 0.5% oxygen (3 mmHg) (Figure 2).

Prior to 1990, information on hypoxia was primarily obtained from excised rodent tumours treated with markers of hypoxia and/or vascular perfusion.⁴ When the Eppendorf electrode became available, it allowed direct oxygen measurement *in situ* and led to many studies which showed conclusively that oxygen levels were severely reduced in human tumours.⁵ The burgeoning interest in hypoxia was further fuelled by the critical finding that hypoxia selects for stress-resistant, more malignant tumour cells.^{6–8} This implied that tumour cells that survive hypoxic stress were likely to be a significant source of viable clonogens that can repopulate tumours with more malignant/metastatic cells. Unfortunately, most treatment

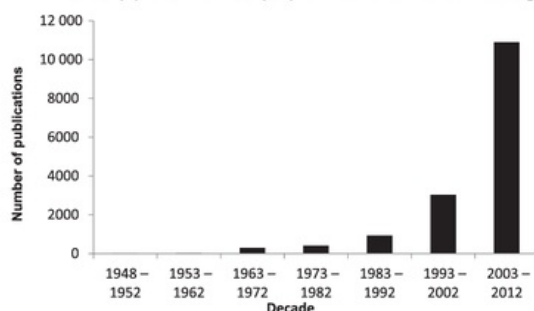
protocols are less effective against hypoxic cells, which are resistant not only to RT but also to standard cytotoxic chemotherapy (CCT);^{9,10} although it has been reported recently that, in a few situations, hypoxia may enhance the effects of CCT.¹¹

DEFINING TUMOUR HYPOXIA

Normoxia and physoxia

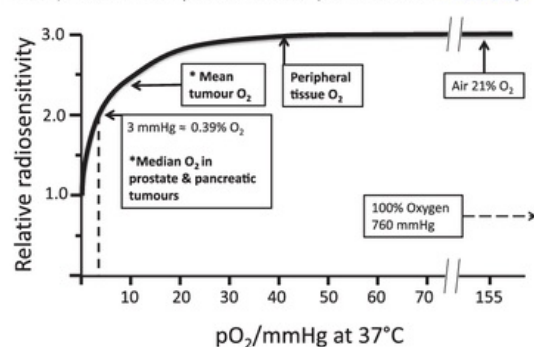
Despite the many studies on tumour hypoxia, there is considerable confusion in the use of the terms “normoxia” and “hypoxia”. Oxygenation measurements in normal tissues show that they exhibit distinct normal ranges, which vary between tissues (Table 1). However, “normoxia” is almost universally used to describe the “normal” oxygen levels in tissue culture flasks, i.e. about 20–21% oxygen (160 mmHg). Although this is not exact, as it is dependent on altitude and added CO₂, for most situations, 20% is a good approximation. Despite the widespread usage of “normoxia”, this is far from an accurate comparator for peripheral tissue oxygenation. Even in lung alveoli, the oxygen level is reduced to about 14.5% oxygen (110 mmHg) by the presence of water vapour and expired CO₂.¹³ It drops further in arterial blood and, by the time it reaches peripheral tissues, the median oxygen levels range from 3.4% to 6.8% with an average of about 6.1% (Table 2).¹³

Figure 1. The number of publications on tumour hypoxia as listed in PubMed, over the previous six decades. [The numbers for 1948–52 (3) and 1953–62 (20) are too small to be visible.]



This clearly highlights the anomaly of the term “normoxia”. Since normal peripheral tissues are exposed to oxygen levels about 75% lower than inspired air, it is proposed that 5% oxygen (38 mmHg) is a more accurate approximation of tissue oxygenation and that this should be recognized as “physoxia” against which other experimental conditions should be compared. Researchers do not accept such an inaccurate value for other parameters such as pH, glucose etc., yet, surprisingly, they ignore the importance of controlling for oxygen, which has been known for many years to be toxic.³⁴ It should be noted that equilibration of culture media to the oxygen level in a specific gassing mixture can take up to 3 h;³⁵ this can be avoided if the gas mixture is in direct contact with the cell monolayer, which can be achieved if cells are grown in oxygen-permeable culture flasks (www.coylelab.com). Since % oxygen is more physiologically meaningful than mmHg, it is proposed that % oxygen is a better unit for reporting oxygen levels as it more adequately illustrates the relatively low, but clearly normal, oxygen levels in many tissues; it also better highlights the particularly low levels of oxygen found in tumours. (Note: the SI unit for gas pressure is kPascal; fortuitously 100% oxygen is equivalent to 101.3 kPascals, so these units are numerically almost equivalent.)

Figure 2. The relation between tissue oxygenation and radiosensitivity. Schematic representation of the radiosensitivity of tissue summarising the data from many sources. (Adapted from Hall and Giaccia³.) *Estimated approximate mean/median from published data (summarized in Table 2).



The lower limit of physoxia is about 3% oxygen (23 mmHg) (Table 1). Homeostasis maintains physiological parameters within tight limits with individual tissues having preferred median oxygen levels (Table 2; see also Carreau et al¹³). This variation suggests that cells of different origins have different oxygen sensitivities, and normal tissues are also known to have a range of tolerances to reducing oxygen. Brain tissue is particularly sensitive and can only survive about 3 min without adequate oxygenation, whereas other tissues are more tolerant, e.g. kidney and liver (15–20 min), skeletal muscle (60–90 min), vascular smooth muscle (24–72 h) and hair and nails (several days).³⁶

Physiological hypoxia

“Physiological hypoxia” can then be defined as the oxygen level at which tissues respond to maintain their preferred oxygen level. This can be by physiological means, e.g. vasodilation, increasing blood flow, and/or upregulation of hypoxia response genes.¹² Since physoxia varies for individual tissues, they are likely to have different hypoxic trigger points below which this occurs. In normal tissues, this will presumably be transitory but sufficient to return the tissue to its preferred oxygen level. However, since normal tissues are ordinarily maintained at 3–7% oxygen, physiological hypoxia is likely to be in the range 2–6% oxygen. This suggests that hypoxia response elements may well upregulate at different oxygen levels in different tissues. Currently, it is difficult to envisage how “physiological hypoxia” can be measured since homeostasis should work to reverse it almost immediately, so any manifestation would be transitory. This will be maintained by a number of changes, including increases in perfusion and temporary stabilization of hypoxia inducible factor (HIF), while readjustments are made.³⁷ When HIF1 α and HIF1 β expression was measured in cultured HeLa cells from 0% to 20% oxygen, a maximal response was found at 0.5% oxygen with a half maximal expression at 1.5–2% oxygen; expression was significantly low above 4% oxygen,³⁸ confirming that HIF1 is active in the required range to control physiological responses to oxygen deprivation (discussed further below).

Pathological hypoxia

Having identified the approximate range of “physiological hypoxia”, this helps to delineate the oxygen levels which are found in pathology. Indeed it begs the question, why in pathological tissues do the homeostatic mechanisms not respond effectively to reverse the falling oxygen levels? In ischaemic disease, which can be either chronic (e.g. in diabetes, reduced lung function etc.) or acute (e.g. stroke, coronary artery occlusion etc.), re-establishment of homeostasis may not be possible owing to the loss/occlusion/reduced flow of vessels feeding the tissue in question. However, in tumours there is often enhanced angiogenesis; yet the oxygen levels (even in untreated tumours) are significantly lower, ranging from 0.3% to 4.2% oxygen (2–32 mmHg), with almost all falling below 2% (Table 2). It is generally recognized that the tumour vasculature is chaotic and is composed of leaky vessels with blind ends, shunts and a tendency to collapse.³⁹ Clearly, the vasculature fails miserably to maintain the oxygen levels, which are well below the adjacent normal tissues (Table 2), despite evidence in many situations that HIF1 is up-regulated.⁴⁰

It is clear, therefore, that tumours are well adapted to grow and expand in this persistently oxygen-depleted tumour micro-environment

Table 1. Approximate levels of oxygen in normal tissues and tumours

mmHg	% Oxygen ^a	Comment
760	100.0	Standard atmospheric pressure
160	21.0	Oxygen in air at normal atmospheric pressure
100	13.5	Inspired oxygen pO ₂ in alveoli; oxygen level affected by in/outflow of gases and water vapour
70	9.5	Arterial blood oxygen concentration
50	6.5	Approximate pO ₂ at venous end of circulation ¹²
Suggested definitions		
38	5.0	Physoxia: physiological oxygen level in peripheral tissues with an average of approximately 6% (ranging from approximately 7.5% to 4% depending on the tissue). For experimental studies, 5% is the proposed compromise since this is often used
15	2.0	Physiological hypoxia ^b —i.e. the lower level at which normal hypoxic responses are elicited (range: lower limit approximately 1%; upper limit possibly $\leq 5\%$)
8	1.0	Pathological hypoxia ^c : shows persistence of poor oxygenation suggesting disruption to normal homeostasis. Below this level pathological hypoxia applies
3	0.4	Radiobiological hypoxia: the oxygen level at which the cytotoxic effect of radiation is half maximal—illustrated in Figure 2

^aIt is impossible to put exact figures on tissue levels. The values provided are a guide derived from several sources (see also Table 2).

^bNormal physiological responses to hypoxia occur above about 15 mmHg (2% oxygen). Normal tissues should not get below this since homeostasis tends to return oxygen levels to physoxia. The exact oxygen level for the upregulation of hypoxia response genes is not known; it may vary between different tissue/cell types since normal tissues have different median oxygen levels.

^cThe presence of pathological hypoxia indicates that the tissue has not been able to revert to physoxia. In normal tissues, persistence of low oxygen will cause tissue necrosis, which can have significant functional consequences. In tumours, this can also happen. Since the tumour is an abnormal growth, loss of tissue through necrosis has no known functional significance. However, hypoxia-resistant tumour cells will initially become quiescent; eventually, there will be selection for hypoxia-tolerant more malignant tumour cells.

(TME). In defining “pathological hypoxia”, there are no absolutes; however, the reality is that all tumours tend to have median tumour oxygen levels $<2\%$ and, within that estimation, individual measurements can vary from about 6% (very rarely) down to zero with a significantly marked skewing towards the lower end of this range; frequently, most values are well below 1.3% oxygen (10 mmHg), especially in the more hypoxic tumours. Many examples of this non-gaussian distribution are found in the publications cited in Table 2.

In tumours, it appears that the homeostatic processes are disrupted for two main reasons. Firstly, the vasculature is of very poor quality and cannot adequately and reliably provide oxygen to the growing tumour. Indeed, if putative tumour cells were sensitive to low oxygen they would die as the oxygen levels are insufficient. This leads to the other main reason: clearly, the tumour cells do not die, showing that a sizeable proportion of them are significantly hypoxia tolerant. In part, this may be attributed to their switch to glycolysis for the supply of most of their energy requirements, a feature of tumours that was identified many years ago by Warburg.⁴¹ In addition, exposure to prolonged pathological hypoxia will select for hypoxia-tolerant tumour cells that are stress resistant and more malignant (see below). It is difficult to be precise about the exact level of oxygen at which this occurs; however, it is almost certainly $<1\%$ oxygen (7.5 mmHg) and may well be significantly lower. It is noteworthy how well tumour cells adapt to significantly low oxygen levels. In one study, hypoxia only caused death of tumour cells when oxygen levels were $<0.01\%$ (0.075 mmHg) for more than 24 h.⁴² In our studies, a proportion

of LNCaP tumour cells survived exposure *in vitro* to 48 h or longer of 0.1% oxygen.⁴³ More recently, we have shown that the median oxygen level of bicalutamide-treated LNCaP prostate xenografts remained below 0.1% oxygen for more than 10 days.⁴⁴ Overall, survival in this extreme stress will drive selection for malignant phenotypes that are governed by a Darwinian selection process.⁴⁵

Variability in tumour oxygenation

Tumour oxygenation is normally reported as a median value; however, there is significant heterogeneity within individual tumours.⁵ In addition, microregional oxygenation is unstable, and oxygen levels fluctuate within the tumour depending on the functionality and proximity of local blood vessels.⁴⁶ Indeed, it has been shown in rat tumours that some of the variation in oxygenation can be attributed to changes in red cell flux.⁴⁷ The “better-oxygenated” tumour cells around functioning capillaries will receive some oxygen, although it is rarely as much as that received by normal cells (Table 2). However, it is sufficient to allow cell division and tumour growth, which is almost certainly boosted by the enhanced level of glycolysis mentioned above.⁴¹ Indeed, it may also be facilitated by an associated reduction in mitochondrial activity.⁴⁸ As the cells divide and move away from the capillaries, they receive less oxygen and the more distal cells are chronically hypoxic;⁴⁹ eventually, the cells die and the tissue becomes necrotic. In histological sections, the viable cells are often seen as “cords” of actively growing cells around perfused blood vessels up to about 150 μm , although this distance is another variable which is variously quoted to range from 70 to 200 μm .^{2,47,50,51} The variability is probably related to two

Table 2. Summary of reported values of the partial pressure of oxygen (pO₂) in human tumours and related normal tissues

Tumour type	<i>n</i>	Median tumour pO ₂	Median % oxygen	<i>n</i>	Median normal tissue pO ₂	Median % oxygen	Fold pO ₂ decrease ^a	Reference
Brain (6)	104	13.0	1.7	104	26.0	3.4	2.0	⁵
Head and neck cancer (13)	592	10.0	1.3		ND	5.9	4.5	⁵
	30	12.2	1.6	14	40.0	5.3	3.3	¹⁴
	23	14.7	1.9	30	43.8	5.8	3.0	¹⁵
	65	14.6	1.9	65	51.2	6.7	3.5	¹⁶
Lung cancer	6	14.3	1.9		ND	5.6	3.0	¹⁷
	20	16.6	2.2		42.8	5.6	2.6	¹⁸
Breast cancer (10)	212	10.0	1.3	212	52.0	6.8	5.2	^{5,19}
Cervical cancer (12)	730	9.0	1.2					⁵
				48	42.0	5.5	4.7	²⁰
Liver	4	6.0	0.8	4	30.0	3.9	5.0	^{21,22}
Pancreatic cancer	7	2.7	0.4	7	51.6	6.8	19.1	²³
	1	2.0	0.3				22.7	²⁴
Prostate cancer	59	2.4	0.3	59	30.0	3.9	12.5 ^b	²⁵
	55	4.5	0.6		ND		6.7 ^b	²⁶
	10	9.4	1.2	2	26.2	3.4	2.8 ^c	²⁷
Vulval cancer	29	11.0	1.4		ND			²⁸
	15	13.0	1.7		ND			²⁹
	19	11.0	1.4		ND			²⁹
	20	10.0	1.3		ND			³⁰
Melanoma	18	11.6	1.5	20	40.5	5.3	3.5	³¹
Renal cell carcinoma	3	10.0	1.3	3	37.6	4.9	3.8	³²
Rectal carcinoma	14	32.0	4.2		52.0	6.8	1.6	^{21,22}
	15	19.0	2.5		52.0	6.8	2.7	³³
Sarcoma (14)	283	14.0	1.8	283	51.0	6.7	3.6	⁵
Averages or total	2257	10.27	1.4	685	45.8	6.0	4.6	
Range of medians		2.0–32.0	0.3–4.2		26.0–51.6	3.4–6.8		

n, number of patients; ND, not determined.

The data included in the table are primarily a summary from a meta-analysis carried out by Vaupel et al.⁵ The number of studies included for each tumour type is indicated by the number in the "tumour type" column. Other data are from single studies, as referenced. The final "average" values for tumour and normal tissue oxygenation are indicative only; they are provided to illustrate the disparity between the two values. The range is considerable and reflects the different tissue origin of the tumours; despite this, there is very limited overlap with the normal tissue data. (The averages were calculated adjusting for the number of values in each cohort.)

^aFold reduction of tumour vs normal tissue is based on all the data presented in the table (except prostate; see further notes).

^bFold reduction calculated on contemporaneous measurements in the psoas muscle.

^cData from a pilot study that included values from the "normal" prostate of two bladder cancer patients.

main factors: (i) the oxygen requirement of a particular tumour cell type and (ii) its hypoxia tolerance. The more metabolically active the cells, the smaller the tumour cords will be. Once the cells become pathologically hypoxic, the proportion of cells in this fraction will depend on their

hypoxia tolerance. The more tolerant they are, the longer they will remain quiescent, yet still viable, resulting in a proportionately more hypoxic tumour with a larger hypoxic fraction. Conversely, hypoxia-sensitive tumour cells will die more quickly, so the hypoxic fraction will be smaller.

Appendix B

MATLAB Code: Renaming files


```

files= dir('H:\ENGG411\DCE_T1-11-03-17-dialysis filter\*.IMA');%its just
assigning the variable a path location
renamed_files= dir('H:\ENGG411\Task3_ConcentrationMap');

%file = dir('/ENGG411/DCE_T1-11-03-17-dialysis filter/');

%copyfile (*.IMA, '/ENGG411/renamed/');
%mkdir ('/ENGG411/renamed/');
%files= dir('*.IMA');

for n = 3:length(files)

    old_name=files(n).name;

    try
        info=dicominfo(['/ENGG411/DCE_T1-11-03-17-dialysis
filter/',old_name]);

        d1=info.PatientName;
        d2=info.SeriesNumber;
        d3=info.InstanceNumber;
        d4=info.AcquisitionTime;
        d5=info.InversionTime;

        if(d5 == 100)
            name = strcat(num2str(d4), '_', num2str(d2), '_', num2str(d5),
'.IMA');
            temp_order = temp_order +1;

            % copyfile (files(n), '/ENGG411/renamed/');
            % if (info.InversionTime >= 30) && (info.InversionTime <=450)
            % if (rem(info.InversionTime-30,20)==0 && info.InversionTime
==100)
                copyfile(fullfile('H:\ENGG411\DCE_T1-11-03-17-dialysis
filter\',old_name), fullfile('H:\ENGG411\Task3_ConcentrationMap',name));
            end
        end
    catch
    end
end

%output_name= strcat(d1, ['_', num2str(d2)], ['_', num2str(d3)]);
%fprintf('output_name');

```


Appendix C

MATLAB Code: Curve fitting and T_1 mapping

```

% In this code, we evaluated T1 Matrix using curve fitting technique

% Step 1: Reading 22 files having signal intensity and each file
% corresponds to different Inversion Time (TI) starting from 30msec to
% 450msec with 20msec intervals

% Step 2: Plotting signal intensity vs inversion time

% Step 3: Curve fitting to find the values of S0 and T1 using the equation
%  $S_i = S_0(1-2\exp(-TI/T_1))$ 

% Step 4: Converting and saving T1 Matrix to DICOM Image File and also,
% saving S0 and T1 matrices as a MAT file

% Step 5: Plotting curve fit and the original data on one graph

% Step 1:
files = (dir('H:\ENGG411\Task2_t1Mapping_noNoise\*.IMA'));

%A = zeros(128*128, 22, 'double');
A = zeros(128*128, 22);
m = 0;
% Need to write a method to only read the files with size of 128x128
for n = 1:22
    file = double(dicomread(files(n).name));
    for x=1:128          % Reading (128,128) matrix each entry
        for y=1:128
            m = m+1;
            A(m,n)= file(x,y)-2048; % This is the signal intensity value
            if(m == 16384)
                m=0;
            end
        end
    end
end
end

% Step 2:
%Plotting a signal intensity vs TI graph
t = 30:20:450;
ti = double(t);

fig01 = figure(1);
plot(t, A(2000,:), 'ro');
xlabel('Inversion Time TI (ms)');
ylabel('Signal Intensity (Si)');
title('Signal Intensity vs Inversion Time at point (15,80)');

fig02 = figure(2);
plot(t, A(5000,:), 'ro');
xlabel('Inversion Time TI (ms)');
ylabel('Signal Intensity (Si)');
title('Signal Intensity vs Inversion Time at point (39,8)');

fig03 = figure(3);
plot(t, A(8000,:), 'ro');

```

```

xlabel('Inversion Time TI (ms)');
ylabel('Signal Intensity (Si)');
title('Signal Intensity vs Inversion Time at point (62,64)');

fig04 = figure(4);
plot(t, A(9000,:), 'ro');
xlabel('Inversion Time TI (ms)');
ylabel('Signal Intensity (Si)');
title('Signal Intensity vs Inversion Time at point (70,40)');

fig05 = figure(5);
plot(t, A(12000,:), 'ro');
xlabel('Inversion Time TI (ms)');
ylabel('Signal Intensity (Si)');
title('Signal Intensity vs Inversion Time at point (93,96)');

% Step 3: Curve Fitting
functn = @(c,ti) c(1)*(1-2*exp(-ti/c(2))); %input function

T_1 = zeros(128, 128); %Matrix to store t1 values
S_0 = zeros(128, 128); %Matrix to store S0 values
x = 1; y = 1; % x and y-coord of t1 matrix
count = 128*128;
%psolve = zeros(128,128);
% m = 1; n = 1;
for i = 1:(128*128)
    B = A(i,:);
    c0 = [500, 2]; %initial guesses for parameters
    %psolve(m, n) = lsqcurvefit(functn, c0, ti, B); %solve for unknowns
    psolve = lsqcurvefit(functn, c0, ti, B);
    if i == 2000
        psolve1 = psolve;
    elseif i == 5000
        psolve2 = psolve;
    elseif i == 8000
        psolve3 = psolve;
    elseif i == 9000
        psolve4 = psolve;
    elseif i == 12000
        psolve5 = psolve;
    end
    S0 = psolve(1); t1 = psolve(2); % solved parameters
    S_0(x,y) = S0; T_1(x,y) = t1;
    y = y + 1;
    if (y ==129)
        y = 1;
        x = x+1;
    end
    count = count -1
end

% Step 4: Converting t1 Matrix to grayScale Image
I = mat2gray(T_1);
% save(T_1);
% save(S_0);

```

```

dicomwrite(I, 't1MappingFinal4.dcm');

% Step 5: Compare raw data to curve fit
vfit = funtn(psolve1, t);
fig06 = figure(6);
plot(ti, A(2000,:), 'bo', t, vfit, 'r.-');
legend('Intensity data (Si)', 'Fit curve');
xlabel('Inversion Time TI (ms)');
ylabel('Signal Intensity (Si)');
title('Signal Intensity vs Inversion Time at point (15,80)');

vfit = funtn(psolve2, t);
fig07 = figure(7);
plot(ti, A(5000,:), 'bo', t, vfit, 'r.-');
legend('Intensity data (Si)', 'Fit curve');
xlabel('Inversion Time TI (ms)');
ylabel('Signal Intensity (Si)');
title('Signal Intensity vs Inversion Time at point (39,8)');

vfit = funtn(psolve3, t);
fig08 = figure(8);
plot(ti, A(8000,:), 'bo', t, vfit, 'r.-');
legend('Intensity data (Si)', 'Fit curve');
xlabel('Inversion Time TI (ms)');
ylabel('Signal Intensity (Si)');
title('Signal Intensity vs Inversion Time at point (62,64)');

vfit = funtn(psolve4, t);
fig09 = figure(9);
plot(ti, A(9000,:), 'bo', t, vfit, 'r.-');
legend('Intensity data (Si)', 'Fit curve');
xlabel('Inversion Time TI (ms)');
ylabel('Signal Intensity (Si)');
title('Signal Intensity vs Inversion Time at point (70,40)');

vfit = funtn(psolve5, t);
fig010 = figure(10);
plot(ti, A(12000,:), 'bo', t, vfit, 'r.-');
legend('Intensity data (Si)', 'Fit curve');
xlabel('Inversion Time TI (ms)');
ylabel('Signal Intensity (Si)');
title('Signal Intensity vs Inversion Time at point (93,96)');

```

Appendix D

MATLAB Code: Concentration map and Dynamic response

```

% image_list= dir('/ENGG411/renamed/')
% image_quantity=size(image_list,1)

%In this code, we find the concentration maps using following steps
% and the equation used is ( $R1 = R1\_0 + rC$ )
%Step 1: we find R1_0 matrix from the T1 matrix.  $R1\_0 = 1/T1$ 

%Step 2: We calculate R1 from  $T1 = 100\text{msec}$  files after the CAgent injected.
%So we'll solve for T1

%Step 3: Find C from the above equation

%Step 4: Find a patch in the middle of the phantom, Average the C values
%for that patch in each file ( where each file corresponds to the different
%time). The patch we picked in the middle has rows from 71 to 95 and
%columns from 50 to 74

files =
(dir('\\\\claudius.science.mq.edu.au\43323774\ENGG411\Task3_ConcentrationMap_2\
*.IMA'));

numOfFiles = size(files,1);
% files(1).name
% files(186).name

%Step 1:
R1_0 = zeros(128, 128, 'double');

for i = 1:128
    for j = 1:128
        R1_0(i,j) = double(1/((T_1(i, j))));
    end
end

%Step 2:
R1 = zeros(numOfFiles, 128,128, 'double');
S_02 = double(S_0);
for n = 1:numOfFiles
    file = dicomread(files(n).name);

    for i = 1:128
        for j = 1:128
            R1 (n,i,j)= log(double((2*S_02(i, j))/(S_02(i, j) -
double(file(i, j))))) /100;
        end
    end
end

%Step 3:
C = zeros(numOfFiles, 128,128, 'double');

for n = 1:numOfFiles
    for i = 1:128
        for j = 1:128

```



```

        C (n,i,j)= (Rl_0(i,j)-Rl(n,i,j))/3;
    end
end
end

t_100 = 10:10:(1860);

fig1 = figure(1);
plot(t_100, C(:,83,62));
xlim([0 2000]);
ylim([-0.007 -0.0035]);
xlabel('Time (s)');
ylabel('Concentration C (mmol/L)');
title('Concentration vs time at point (83,62)');

fig2 = figure(2);
plot(t_100, C(:,59,62));
xlim([0 2000]);
ylim([-0.007 -0.0035]);
xlabel('Time (s)');
ylabel('Concentration C (mmol/L)');
title('Concentration vs time at point (59,62)');

fig3 = figure(3);
plot(t_100, C(:,83,86));
xlim([0 2000]);
ylim([-0.007 -0.0035]);
xlabel('Time (s)');
ylabel('Concentration C (mmol/L)');
title('Concentration vs time at point (83,86)');

fig4 = figure(4);
plot(t_100, C(:,107,62));
xlim([0 2000]);
ylim([-0.007 -0.0035]);
xlabel('Time (s)');
ylabel('Concentration C (mmol/L)');
title('Concentration vs time at point (107,62)');

fig5 = figure(5);
plot(t_100, C(:,83,38));
xlim([0 2000]);
ylim([-0.007 -0.0035]);
xlabel('Time (s)');
ylabel('Concentration C (mmol/L)');
title('Concentration vs time at point (83,38)');

%Step 4: Dynamic Map (Average Concentration) for 5 points
C_Dynamic = zeros(numOfFiles, 5);
sum = 0;

%First Dynamic map C_Dynamic(n,1)
for n = 1:numOfFiles
    for i = 71:95
        for j = 50:74

```

```

        sum = sum + C(n,i,j);
    end
end
C_Dynamic(n,1)= sum/625;
sum =0;
end

%Second Dynamic map C_Dynamic(n,2)
for n = 1:numOfFiles
    for i = 53:65
        for j = 56:68
            sum = sum + C(n,i,j);
        end
    end
    C_Dynamic(n,2)= sum/169;
    sum =0;
end

%Third Dynamic map C_Dynamic(n,3)
for n = 1:numOfFiles
    for i = 77:89
        for j = 80:92
            sum = sum + C(n,i,j);
        end
    end
    C_Dynamic(n,3)= sum/169;
    sum =0;
end

%Fourth Dynamic map C_Dynamic(n,4)
for n = 1:numOfFiles
    for i = 101:113
        for j = 56:68
            sum = sum + C(n,i,j);
        end
    end
    C_Dynamic(n,4)= sum/169;
    sum =0;
end

%Fifth Dynamic map C_Dynamic(n,5)
for n = 1:numOfFiles
    for i = 77:89
        for j = 32:44
            sum = sum + C(n,i,j);
        end
    end
    C_Dynamic(n,5)= sum/169;
    sum =0;
end

fig6 = figure(6);
plot(t_100, C_Dynamic(:,1));
xlim([0 2000]);
ylim([-0.007 -0.0035]);
xlabel('Time (s)');

```

```

ylabel('Concentration C (mmol/L)');
title('Dynamic Map (Concentration Avg.) centred at point (83,62)');

fig7 = figure(7);
plot(t_100, C_Dynamic(:,2));
xlim([0 2000]);
ylim([-0.007 -0.0035]);
xlabel('Time (s)');
ylabel('Concentration C (mmol/L)');
title('Dynamic Map (Concentration Avg.) centred at point (59,62)');

fig8 = figure(8);
plot(t_100, C_Dynamic(:,3));
xlim([0 2000]);
ylim([-0.007 -0.0035]);
xlabel('Time (s)');
ylabel('Concentration C (mmol/L)');
title('Dynamic Map (Concentration Avg.) centred at point (83,86)');

fig9 = figure(9);
plot(t_100, C_Dynamic(:,4));
xlim([0 2000]);
ylim([-0.007 -0.0035]);
xlabel('Time (s)');
ylabel('Concentration C (mmol/L)');
title('Dynamic Map (Concentration Avg.) centred at point (107,62)');

fig10 = figure(10);
plot(t_100, C_Dynamic(:,5));
xlim([0 2000]);
ylim([-0.007 -0.0035]);
xlabel('Time (s)');
ylabel('Concentration C (mmol/L)');
title('Dynamic Map (Concentration Avg.) centred at point (83,38)');

%Comparison plots: concentration at a point and Avg. Concentration (Dynamic
%Response)
fig11 = figure(11);
plot(t_100, C_Dynamic(:,1));
hold on
plot(t_100, C(:,83,62));
hold off
xlim([0 2000]);
ylim([-0.007 -0.0035]);
xlabel('Time (s)');
ylabel('Concentration C (mmol/L)');
title('Comparison of Concentration and Dynamic Map centred at point
(83,62)');
legend('Avg. Concentration (Dynamic response)', 'Concentration at the centered
point');

fig12 = figure(12);
plot(t_100, C_Dynamic(:,2));
hold on

```

```

plot(t_100, C(:,59,62));
hold off
xlim([0 2000]);
ylim([-0.007 -0.0035]);
xlabel('Time (s)');
ylabel('Concentration C (mmol/L)');
title('Comparison of Concentration and Dynamic Map centred at point
(59,62)');
legend('Avg. Concentration (Dynamic response)', 'Concentration at the centered
point');

fig13 = figure(13);
plot(t_100, C_Dynamic(:,3));
hold on
plot(t_100, C(:,83,86));
hold off
xlim([0 2000]);
ylim([-0.007 -0.0035]);
xlabel('Time (s)');
ylabel('Concentration C (mmol/L)');
title('Comparison of Concentration and Dynamic Map at point (83,86)');
legend('Avg. Concentration (Dynamic response)', 'Concentration at the centered
point');

fig14 = figure(14);
plot(t_100, C_Dynamic(:,4));
hold on
plot(t_100, C(:,107,62));
hold off
xlim([0 2000]);
ylim([-0.007 -0.0035]);
xlabel('Time (s)');
ylabel('Concentration C (mmol/L)');
title('Comparison of Concentration and Dynamic Map at point (107,62)');
legend('Avg. Concentration (Dynamic response)', 'Concentration at the centered
point');


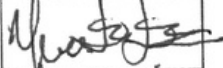

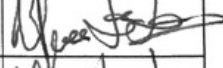









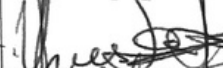





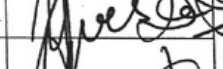
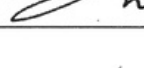

fig15 = figure(15);
plot(t_100, C_Dynamic(:,5));
hold on
plot(t_100, C(:,83,38));
hold off
xlim([0 2000]);
ylim([-0.007 -0.0035]);
xlabel('Time (s)');
ylabel('Concentration C (mmol/L)');
title('Comparison of Concentration and Dynamic Map at point (83,38)');
legend('Avg. Concentration (Dynamic response)', 'Concentration at the centered
point');

```

Appendix E

Consultation Meetings Attendance Form

Consultation Meetings Attendance Form

Week	Date	Comments (if applicable)	Student's Signature	Supervisor's Signature
PRE-PROJECT	9/2/17	Discussion about project and theory		
WEEK 4	21/3/17	meeting with Mahdiah - Discussion about results		
MID-SEM Break	19/4/17	meeting with Mahdiah - Discussion about MATLAB based		
MID-SEM Break	27/4/17	Project update with Yves.		
WEEK 8	4/5/17	meeting with Yves - Discussion about T1 mapping.		
WEEK 9	10/5/17	meeting with Mahdiah - programming doubts		
WEEK 10	17/5/17	meeting with Yves - Oxygen conc. maps Qs		
WEEK 11	22/5/17	meeting with Yves - Report structure		
WEEK 11	26/05/17	meeting with Mahdiah		
WEEK 12	29/05/17	meeting with Yves - Project update.		
WEEK 12	30/05/17	meeting with Yves		
WEEK 12	1/06/17	meeting with Yves	